Ion-Mediated Nucleic Acid Helix-Helix Interactions

Zhi-Jie Tan and Shi-Jie Chen
Department of Physics and Astronomy and Department of Biochemistry, University of Missouri, Columbia, Missouri

ABSTRACT Salt ions are essential for the folding of nucleic acids. We use the tightly bound ion (TBI) model, which can account for the correlations and fluctuations for the ions bound to the nucleic acids, to investigate the electrostatic free-energy landscape for two parallel nucleic acid helices in the solution of added salt. The theory is based on realistic atomic structures of the helices. In monovalent salt, the helices are predicted to repel each other. For divalent salt, while the mean-field Poisson-Boltzmann theory predicts only the repulsion, the TBI theory predicts an effective attraction between the helices. The helices are predicted to be stabilized at an interhelix distance ~26–36 Å, and the strength of the attractive force can reach $-0.37\ k_BT$/bp for helix length in the range of 9–12 bp. Both the stable helix-helix distance and the strength of the attraction are strongly dependent on the salt concentration and ion size. With the increase of the salt concentration, the helix-helix attraction becomes stronger and the most stable helix-helix separation distance becomes smaller. For divalent ions, at very high ion concentration, further addition of ions leads to the weakening of the attraction. Smaller ion size causes stronger helix-helix attraction and stabilizes the helices at a shorter distance. In addition, the TBI model shows that a decrease in the solvent dielectric constant would enhance the ion-mediated attraction. The theoretical findings from the TBI theory agree with the experimental measurements on the osmotic pressure of DNA array as well as the results from the computer simulations.

INTRODUCTION

Nucleic acids (DNAs and RNAs) are highly charged polyanionic chain molecules. The folding of nucleic acids requires the cations to neutralize the negative backbone charges. Therefore, the solvent ionic conditions, including salt concentration, ionic charge and size, solvent dielectric constant, and temperature play essential roles in the folding of nucleic acids (1–10).

Despite the extensive experimental and theoretical studies (11–19), our ability to make accurate quantitative predictions for the ion effects on the folding of complex secondary structures is quite limited, especially in multivalent metal ion solutions. Even if the ion-dependence of the secondary structure folding can be accurately predicted, we are still unable to quantitatively understand how ions assist the extended secondary structural segments to fold up into the compact tertiary structures. Experiments have shown that nucleic acid (RNA) folding undergoes a collapse process (20–28), where the secondary structural segments (e.g., helices) approach each other to form a compact state. A rudimentary process in chain collapse is the aggregation of helices. In this study, we investigate how the metal ions assist the folding (aggregation) of two finite-length helices and how the different ionic conditions affect the helix-helix electrostatic interactions. Since helix-helix recognition is a fundamental tertiary interaction in nucleic acids, this study may provide a paradigm for the ion-assisted nucleic acid tertiary interactions.

For RNAs, various experiments have shown that multivalent ions are efficient to cause chain compaction (20–28). Among other forces, the cation-mediated electrostatic helix-helix attraction can be a possible candidate for the driving force to cause the collapse of RNAs (20–22). Experiments have been designed to probe the driving force for RNA collapse in order to shed light on the mechanism of RNA compaction (28,29). In addition, DNAs, which are long polyanionic molecules, need to condense into compact particles in cells. DNA condensation, a process similar to RNA compaction, has been studied for over two decades (30–40). Experimental and theoretical studies suggest that a possible driving force for DNA helix-helix attraction may come from the correlated multivalent cations (30–40). In addition, for other polyelectrolyte molecules, such as F-actin, filamentous viruses fd and M13, and nucleosomes, experiments have shown the similar multivalent ion-induced collapse (aggregation) (41–47).

Parallel to the experimental development, different theories and computational models have been developed to treat the helix-helix electrostatic interaction. There have been primarily two types of polyelectrolyte theories used to treat helix-helix interactions: the Poisson-Boltzmann (PB) theory (48–55) and the counterion condensation (CC) theory (56). Both theories have been very useful in predicting many thermodynamic properties of nucleic acids and proteins in salt solutions. For the helix-helix interaction, however, the PB theory, which ignores the interion correlations, predicts only repulsive force (57). In contrast, the CC theory predicts attractive forces in both monovalent and multivalent ion solutions and the CC theory attributes the attraction to the increased ion entropy (58–61).

Computer simulations have shown that attraction occurs only in the presence of multivalent ions (62–72). Models based on the simplified structures of the helices (in an asymptotically dilute salt solution) suggest that the attraction may arise from the correlated ion configurations on the surface of

Submitted March 1, 2006, and accepted for publication April 14, 2006.
Address reprint requests to Shi-Jie Chen, E-mail: chenshi@missouri.edu.

0006-3495/06/07/518/19 $2.00
doi: 10.1529/biophysj.106.084285

the approaching polyelectrolytes (73–82). When two highly charged polyelectrolytes (helices) approach each other, the strong electric field drives the ions between the helices to self-organize in order to lower the total energy. In the low-temperature limit, the strongly correlated ions can form a Wigner crystal-like configuration and the attraction between two polyelectrolytes can be strong. As the temperature is increased, the Wigner crystal-like ion configuration would be disrupted gradually and the strength of attraction decreases. Both experiments (38,46) and computer simulations (63,66, 69,79) have suggested the existence of the correlated states of the ions. However, the simplified models cannot treat detailed helix structure, which can be essential in the quantitative prediction of the interhelix force. In this study, we aim to obtain a detailed microscopic picture for the ion-mediated helix-helix interaction for realistic nucleic acid helix structures.

Recently, we developed a statistical mechanical theory (denoted the tightly bound ion theory, abbreviated as TBI theory) for nucleic acid molecules. An advantage of the theory is that it can explicitly account for the correlations and the fluctuations for bound ions near the molecule surface (83). As tested against experiments, computer simulations, and the PB and the CC theories (83), the TBI theory gives reliable ion-dependent predictions such as the ion dependence of the helix-coil transition for DNA in both NaCl and $MgCl_2$ solutions (84). In this study, we apply the TBI theory to investigate the ion-mediated nucleic acid helix-helix interactions. Compared with the previous simplified models, the present TBI theory (83,84) is based on realistic helical structure at the atomic level and can treat the dependence on the charge, the concentration, and the size of the added salt ions in the supporting solutions. Moreover, the present model can account for the different binding modes of the bound ions and the fluctuations of the binding modes and the electrostatic and excluded volume correlations between the bound ions. The fluctuations and correlations can play significant roles for multivalent ions such as Mg^{2+} ion solution.

In this work, based on the TBI theory, we calculate the electrostatic free energy for two parallel nucleic acid helices of finite length in the presence of monovalent or divalent salt solutions. We investigate how the helix-helix interaction depends on the ion valency, ion size, ion concentration, and solvent dielectric constant. We also analyze the driving force for the ion-mediated helix-helix attraction. In addition, we compare the predictions with the experimental measurements on osmotic pressure of DNA array as well as with Monte Carlo simulations.

THEORY AND METHODS

Tightly bound ions and tightly bound region

The primary motivation to develop the tightly bound ion (TBI) theory is to go beyond the mean-field approach by treating the ion correlation and fluctuation effects for polyelectrolyte systems (83,84). The basic idea is to classify two types of ions according to ion-ion correlation strength: the (strongly correlated) tightly bound ions and the (weakly correlated) diffusively bound ones. Correspondingly, the solution can be divided into two regions: the tightly bound region and the diffusively bound region. The motivation to distinguish the two types of ions is to treat them separately. For the (weakly correlated) diffusively bound ions, we use PB; for the (strongly correlated) tightly bound ions, we use a separate treatment to explicitly account for the ion correlations and fluctuations.

The tightly/diffusively bound regions are determined by the ion-ion correlation condition. We consider 1), the electrostatic correlation, measured by the parameter $\Gamma(\mathbf{r})$,

$$\Gamma(\mathbf{r}) = \frac{(zq)^2}{\epsilon a_{ws}(\mathbf{r}) k_B T}, \tag{1}$$

and 2), the excluded volume correlation, measured by the ion radius r_c and the Wigner-Seitz radius $a_{ws}(\mathbf{r})$ (83,84). In Eq. 1, $\mathbf{r}$ is the position vector, zq is the charge of cations, ϵ is the dielectric constant of solute, and $a_{ws}(\mathbf{r})$ is the Wigner-Seitz radius, which is given by the cation concentration $c(\mathbf{r})$ in excess of the bulk concentration c^0 (73),

$$\frac{4\pi}{3}[a_{ws}(\mathbf{r})]^3[c(\mathbf{r}) - c^0] = 1. \tag{2}$$

The tightly bound region is defined as position $\mathbf{r}$ such that either $\Gamma(\mathbf{r})$ is larger than a critical value Γ_c so the Coulombic correlation is strong, or $a_{ws}(\mathbf{r})$ is smaller than $(r_c + \Delta r)$ so ions are so crowded that they can easily bump into each other (83,84):

$$\Gamma(\mathbf{r}) \geq \Gamma_c; 2a_{ws}(\mathbf{r}) \leq 2(r_c + \Delta r). \tag{3}$$

Here, Δr is the mean displacement of ions deviating from their equilibrium positions, and $2(a_{ws}(\mathbf{r}) - \Delta r)$ is the closest distance of approach between two ions before they overlap.

Equation 3 gives the criteria to characterize the strong Coulombic and excluded volume correlations, respectively. The value Γ_c is chosen to be 2.6, the critical value for the gas-liquid transition point in ionic systems (85–87), and $\Delta r/d \simeq 0.1$ is used as the melting point for the correlated structure according to Lindemann's melting theory (88–90).

As an approximation, we compute $c(\mathbf{r})$ using the nonlinear PB equation

$$\nabla \cdot \epsilon_0 \epsilon \nabla \psi(\mathbf{r}) = -4\pi \left\{ \rho_f + \sum_\alpha z_\alpha q c_\alpha(\mathbf{r}) \right\}; \tag{4}$$

$$c_\alpha(\mathbf{r}) = c_\alpha^0 e^{-z_\alpha q \psi(\mathbf{r})/k_B T}, \tag{5}$$

where α denotes the ion species, $z_\alpha q$ is the charge of the ion, and c_α^0 is the bulk ion concentration. The value ρ_f is the charge density for the fixed charges, ϵ_0 is the permittivity of free space, and $\psi(\mathbf{r})$ is the electrostatic potential at $\mathbf{r}$. From $c(\mathbf{r})$ and Eq. 3, we can unambiguously define the tightly bound region (83,84). In Fig. 1 we show examples of the tightly bound regions around two parallel DNA helices separated at different distances.

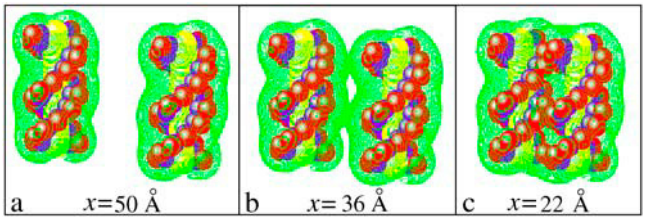

FIGURE 1 The tightly bound regions around two parallel 12-bp B-DNA helices in a divalent ion solution with different interaxis separations: (*a*) 50 Å; (*b*) 36 Å; and (*c*) 22 Å. The divalent salt concentration is 0.1 M and the cation radius is 3.5 Å. The red spheres represent the phosphate groups and the green dots represent the points at the boundaries of the tightly bound regions. The B-DNA helices are produced from the grooved primitive model (83,84,118).

Partition function

For two N-bp double-stranded nucleic acid molecules, there are a total of $4N$ phosphates. We divide the whole tightly bound region into $4N$ cells, each around a phosphate. In a tightly bound cell, say, the i^{th} cell, there can exist $m_i = 0, 1, 2\ldots$ tightly bound ions. The set of the $4N$ numbers $\{m_1, m_2, \ldots, m_{4N}\}$ defines a binding mode for the system of two N-bp helices. A large number of such binding modes exist. The total partition function of the system is given by the sum over all the possible binding modes M,

$$Z = \sum_{M} Z_M, \tag{6}$$

where Z_M is the partition function for a given binding mode M (83,84),

$$Z_M = Z^{(id)} c_+^{N_b} \left(\int \prod_{i=1}^{N_b} d\mathbf{R}_i \right) e^{-G_E^b/k_BT} e^{-G_E^d/k_BT} e^{-G_S^d/k_BT}. \tag{7}$$

Here, $Z^{(id)}$ is the partition function for the uniform solution without the polyelectrolyte. The value c_+ denotes the total counterion concentration. The value N_b is the number of tightly bound ions for the mode M, and $\mathbf{R}_i$ denotes the position of the i^{th} bound ion. The configurational integral

$$\int \prod_{i=1}^{N_b} d\mathbf{R}_i$$

provides a measure for the free accessible space for the N_b tightly bound ions.

Throughout the article, we use the following conventions for the notations:

- Superscripts *b*, *d*, and *tot* denote the tightly bound ions, the diffuse ions, and the total (bound and diffuse) ions, respectively;
- Subscripts *E* and *S* denote the energy (enthalpy) and the entropic free energy ($-TS$, where S is the entropy), respectively;
- Over-lines denote the statistical average over all the possible binding modes.

In Eq. 7, G_E^b, G_E^d, and G_S^d are the energies of the bound ions, of the diffuse ions, and the entropy of the diffuse ions, respectively. In what follows, we present a brief account of the theory for the computation of G_E^b, G_E^d, and G_S^d.

The value G_E^b in Eq. 7 is the mean Coulombic interaction energy between all the charge-charge pairs (including the phosphate groups and the tightly bound ions) in the tightly bound region (83,84),

$$G_E^b \simeq \sum_i \Phi_1(i) + \sum_{ij} \Phi_2(i,j), \tag{8}$$

where $\Phi_1(i)$ is the potential of mean force for the Coulomb interactions between charges within a tightly bound cell i, and $\Phi_2(i, j)$ is for the interactions between charges in different tightly bound cells i and j. For the two-helix system, i and j can be the tightly bound cells in the same helix or in different helices. Since the interactions between the cells in different helices is dependent on the interhelix separation x, the potential of mean force $\Phi_2(i, j)$ is x-dependent if i and j are for different helices.

$\Phi_1(i)$ and $\Phi_2(i, j)$ are calculated as the average over all the possible positions $\mathbf{R}$ of the tightly bound ions in the respective cells (83,84),

$$\Phi_1(i) = -k_B T \ln\langle e^{-u_{ii}(\mathbf{R}_i)/k_BT}\rangle;$$
$$\Phi_2(i,j) = -k_B T \ln\langle e^{-u_{ij}(\mathbf{R}_i,\mathbf{R}_j)/k_BT}\rangle, \tag{9}$$

where u_{ii} represents the Coulomb interactions between the charges in cell i, and u_{ij} the interactions between the charges in different cells i and j.

The value G_E^d in Eq. 7 is the free energy for the electrostatic interactions between the diffusive ions and between the diffusive ions and the charges in the tightly bound region. The value G_S^d in Eq. 7 is the entropic free energy of the diffusive ions. With the mean-field approximation for the diffusive ions (91,92), G_E^d and G_S^d can be calculated from these equations (83,84),

$$G_E^d = \frac{1}{2} \int \sum_\alpha c_\alpha(\mathbf{r}) z_\alpha q[\psi(\mathbf{r}) + \psi'(\mathbf{r})] d^3\mathbf{r}, \tag{10}$$

$$G_S^d = k_B T \int \sum_\alpha \left[c_\alpha(\mathbf{r}) \ln \frac{c_\alpha(\mathbf{r})}{c_\alpha^0} - c_\alpha(\mathbf{r}) + c_\alpha^0 \right] d^3\mathbf{r}, \tag{11}$$

where $\psi'(\mathbf{r})$ is the electrostatic potential for system without the diffusive salt ions. The value $\psi'(\mathbf{r})$ is used here because $\psi(\mathbf{r})$–$\psi'(\mathbf{r})$ gives the contribution to the electrostatic potential from the diffusive ions. The values $\psi(\mathbf{r})$ and $\psi'(\mathbf{r})$ are obtained from the nonlinear PB (Eq. 4, with salt) and the Poisson equation (salt-free), respectively.

From the above expressions, we can calculate the partition function Z, from which we obtain the electrostatic free energy G for the system:

$$G = -k_B T \ln (Z/Z^{(id)}) = -k_B T \ln \sum_M (Z_M/Z^{(id)}). \tag{12}$$

Moreover, from the mode probability

$$p_M = \frac{Z_M}{Z} \tag{13}$$

we can calculate the mean electrostatic interaction $\overline{G_E^{tot}}$,

$$\overline{G_E^{tot}} = \sum_M (G_E^b + G_E^d) p_M, \tag{14}$$

and the entropic free energy $\overline{G_S^{tot}}$,

$$\overline{G_S^{tot}} = G - \overline{G_E^{tot}}. \tag{15}$$

Furthermore, we can decompose $\overline{G_S^{tot}}$ into contributions from the diffusive ions

$$\overline{G_S^d} = \sum_M (G_S^d) p_M, \tag{16}$$

and from the (tightly) bound ions

$$\overline{G_S^b} = \overline{G_S^{tot}} - \overline{G_S^d}. \tag{17}$$

The above classification for the enthalpy and entropy is based on several approximations. First, the electrostatic energy and entropy of the ions in solution are coupled to the dielectric property of the solvent, which, in the continuum solvent model, is represented by the dielectric constant. The dielectric constant is intrinsically related to the solvent entropy. Therefore, G_E^d, the energy of the diffuse ions, implicitly contains the solvent entropy. Second, for each given ion-binding mode, the energy G_E^b of the bound ions is computed as an average over the different configurations of the bound ions within the respective tightly bound cells. Therefore, G_E^b contains the configurational entropy effect for the tightly bound ions. Besides the solvent entropy, the entropic free energy $\overline{G_S^d}$ for the diffuse ions accounts for the translational entropy of the diffuse ions, and $\overline{G_S^b}$ for the bound ions includes the combinatory entropy of the different binding modes as well as the configurational entropy of the tightly bound ions.

Numerical computation

The computation of the electrostatic free energy for two helices with the TBI theory can be summarized in the following steps (83,84).

First, we solve the nonlinear PB (Eq. 4) to obtain the ion distribution $c(\mathbf{r})$ for the two-helix system (83,84), from which we determine the tightly bound region using Eq. 3.

Second, we compute the pairwise potential of mean force $\Phi_1(i)$ and $\Phi_2(i, j)$ for different tightly bound cells (i and j values) from Eq. 9 by averaging over all the possible positions of the tightly bound ions inside the respective tightly bound cells. In the calculations for Φ_1 and Φ_2, the excluded volume

effects between ions and between ions and helices are accounted for by using a Lennard-Jones potential:

$$V_{LJ} \propto \begin{cases} (r/r_0)^{-12} - 2(r/r_0)^{-6} + 1 & \text{for} \quad r < r_0; \\ 0 & \text{for} \quad r \geq r_0, \end{cases}$$

where r is the distance between the centers of ions and r_0 is the sum of the radii for the two spheres. Clearly the potentials of mean force are dependent on the detailed structure of the molecules (helices) and the size (and shape) of the ions. The calculated potentials of mean force are tabulated and stored for the calculations of partition function.

Third, we enumerate the binding modes and for each mode, we calculate G_E^b, G_E^d, and G_S^d from Eqs. 8–11. Summation over the binding modes gives the total partition function Z (Eq. 6), from which we can calculate the electrostatic free energy for the helices. For long helices, there are a large number of binding modes, therefore, a brute-force exhaustive enumeration for all the modes is practically impossible. So we have developed a special numerical method to efficiently treat long helices by using a coarse-grained approximation for the low-probability (i.e., small p_M) modes. The details of the method are given in Appendix A.

RESULTS AND DISCUSSION

In this work, we focus on DNA helices. The same method and the physical mechanisms revealed here may also be applicable to RNA helices. To investigate the possible attraction between finite-length helices, we choose a model system with two parallel helices, each of length equal to one helix pitch. We compute the free energy $G(x)$ of the system as a function of the interhelix distance x. We use $\Delta G(x)$ to denote the free energy change of the system as the helices approach each other from ∞ far apart,

$$\Delta G(x) = G(x) - G(\infty), \tag{18}$$

where $G(x)$ and $G(\infty)$ are determined from Eq. 12. We treat $x = 50$ Å as the outer reference distance (for separated DNA helices), i.e., we treat $G(50$ Å$)$ as $G(\infty)$. Our control test shows that the results are not sensitive to the choice of the large reference distance 50 Å.

In this section, we use the TBI theory to analyze the general mechanism for the possible attraction between two helices in the presence of divalent salt ions. We then investigate how the ion valency, ion concentration, ion size, and solvent dielectric constant affect the helix-helix interactions. In the next section, we calculate the osmotic pressure of DNA aggregated array and compare our predictions with the experimental measurements.

Driving force for ion-mediated helix-helix attraction

The predicted free energy $\Delta G(x)$ is shown as a function of the interhelix separation x in Fig. 2 for 0.01 M divalent salt. The free energy landscape $\Delta G(x)$ shows that the two helices attract each other for $x \gtrsim 28$ Å and the most stable helix-helix configuration occurs at $x \simeq 28$ Å, where the free energy minimum is located. The results from the free energy landscape are in accordance with the previous findings that divalent ions can induce macroion-macroion attractions (62–82).

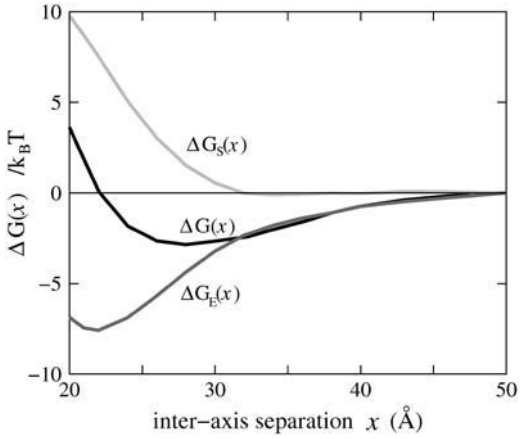

FIGURE 2 The free energy $\Delta G(x)$, the electrostatic energy $\Delta G_E(x)$, and the entropic free energy $\Delta G_S(x)$, calculated from the TBI theory, as functions of the interhelix separation x for 0.01 M divalent salt concentration. The minimum contact distance for parallel helices is $\sim x \simeq 20$ Å.

Is the ion-mediated attraction entropically or enthalpically driven? To answer this question, we calculate the total electrostatic energy ΔG_E and the total entropic free energy ΔG_S,

$$\Delta G_E(x) = \overline{G_E^{tot}(x)} - \overline{G_E^{tot}(50\,\text{Å})};$$
$$\Delta G_S(x) = \overline{G_S^{tot}(x)} - \overline{G_S^{tot}(50\,\text{Å})}, \tag{19}$$

from Eqs. 14 and 15, respectively. Fig. 2 shows that, when the two helices approach each other from ∞, $\Delta G_E(x)$ decreases until $x \simeq 22$ Å. Thus, $\Delta G_E(x)$ tends to give an attractive force for $x \gtrsim 22$ Å. On the other hand, as the two helices approach each other, $\Delta G_S(x)$ increases and thus tends to give a repulsive force. Therefore, the helix-helix attraction comes from the electrostatic energy $\Delta G_E(x)$; i.e., the attraction is enthalpically driven.

To understand the physical mechanism for the interhelix interaction, we examine the distance-dependence of the (bound) ion distribution and the free energy of the system. For large helix-helix separation, the helices and the associated bound ions are nearly independent with each other and the interhelix correlation is weak. The close approach between the two helices causes the following two effects.

First, in response to the enhanced electric field, more ions become tightly bound, causing a stronger charge neutralization (charge screening) for the polyanionic helices. This would weaken the average tendency of the repulsion between the two likely charged helices.

Second, the correlation between the tightly bound ions on the different helices becomes stronger. The (correlated) bound ions can self-organize to form the correlated low-energy states. Such correlated states can reach much lower energies than the (uncorrelated) mean-field states. So the interhelix correlation can cause a rapid decreasing of the electrostatic energy $\Delta G_E(x)$ as x is decreased. This leads to an attraction between the helices.

In the correlated low energy states, the bound (divalent) ions tend to reside in the region of the lowest electric potential produced by all the bound and the diffusive ions as well as the phosphates on both helices. Shown in Fig. 3 are representative (most probable) low-energy binding modes and the mean charge neutralization for different phosphates for $x =$ 24 Å and 50 Å. From the (most probable) bound ion distribution for $x = 24$ Å, we find that the strongest correlation occurs between ions bound to phosphates that are directly facing each other, such as phosphates P_1 and P_2 in Fig. 3. To more efficiently lower the energy, ions have higher tendency to bind to these phosphates and the ion-binding to these phosphates is highly correlated. The most probable (lowest energy) binding mode gives a strong attractive force. For the binding mode depicted in Fig. 3 *a*, phosphate P_1 bound by a divalent cation would attract the negatively charged unbound phosphate P_2. The statistical ensemble-averaged, mean-binding mode indicates that ions prefer to bind to the region between the two helices so as to interact with both helices strongly.

There exist a large number of ion binding modes with low-lying energies. These modes represent the correlated fluctuations of the ion-binding state. The multiplicity of these low-lying energy modes makes significant contributions to the helix-helix attraction.

In addition, as the helices approach each other, more ions become tightly bound and hence the ion entropy would decrease and the entropic free energy $\Delta G_S(x)$ would increase. The competition between the decreasing (attractive) $\Delta G_E(x)$ and the increasing (repulsive) $\Delta G_S(x)$ results in an overall net decreasing (attractive) $\Delta G(x)$.

In the following sections, we show how the ion valency, ion concentration, ion size, and solvent dielectric constant affect the energy component $\Delta G_E(x)$ and the entropy component $\Delta G_S(x)$ and the shape of the free energy landscape for the interhelix interactions.

Ion valency effect on helix-helix interaction

Monovalent and divalent ions have contrasting effects on the helix-helix interaction. The values $\Delta G(x)$ of the systems with monovalent and divalent salts are shown in Fig. 4, *a* and *b*, as functions of the interhelix distance x. As a comparison, the predictions from the TBI theory and from the PB theory are both shown in the figures. For monovalent salt, the TBI theory and the PB give nearly identical results for $\Delta G(x)$, and both PB and TBI theories predict only repulsive helix-helix interaction. For divalent salt, however, the TBI theory predicts an effective attraction between the two helices, while PB predicts a repulsive force. The different results for monovalent and divalent ions clearly show the role of the ion valency in helix-helix interaction. The findings from the TBI theory agree with the findings from the previous experiments (30–34), computer simulations (62–72), and theoretic analysis (73–82).

For monovalent salt, where ion-ion correlation is weak, there are only very small amounts of (strongly correlated) tightly bound ions. Consequently, PB and TBI theories give similar results. For divalent salt, the ion-ion correlation can be strong and there can be a significant amount of tightly bound ions, so the PB theory, which neglects the interion correlations, cannot provide an accurate description for the system. In contrast, the TBI theory can explicitly account for the ion-binding correlations and fluctuations and allows the tightly bound ions to self-organize into correlated configurations (83,84). As a result, TBI predicts a much lower free energy than the mean-field theory, especially for the short interhelix distance, where the correlation effect is strong.

To gain more detailed insights into the ion valency effect on helix-helix interaction, we analyze the components of the free energy $\Delta G(x)$: the electrostatic energy $\Delta G_E(x)$ and the entropic free energy $\Delta G_S(x)$ (see Eq. 19). Fig. 4, *c* and *d*, show $\Delta G_E(x)$ and $\Delta G_S(x)$ as functions of the interhelix separation x for monovalent and divalent salts, respectively.

For the entropic free energy $\Delta G_S(x)$, as the two helices approach each other, in general, the stronger electric field (for smaller x) around the polyanionic helices drives more cations to bind to the helix (especially between the two helices), which results in a decrease in the entropy of the ions and thus an increase in the entropic free energy $\Delta G_S(x)$. In particular, when the helices are very close to each other ($x \sim$20–30 Å), the strong electric potential between the polyanionic helices would significantly restrict the freedom of the bound ions and thus cause a rapid decrease of ion entropy and hence a rapid rise of $\Delta G_S(x)$.

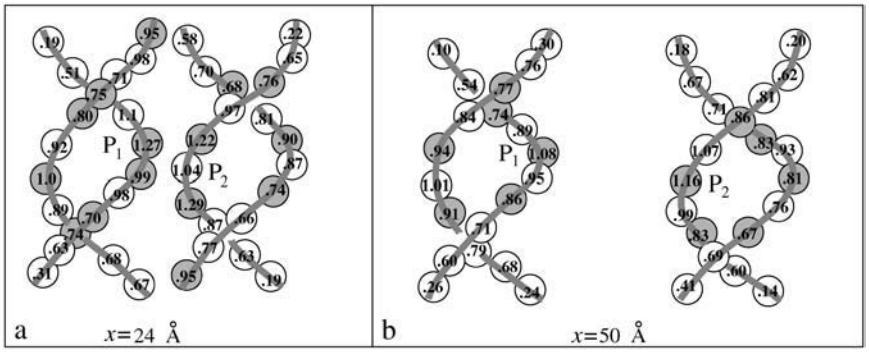

FIGURE 3 Illustrations for divalent ion binding to two parallel DNA helices for different interaxis separations: (*a*) $x = 24$ Å and (*b*) $x = 50$ Å. The circles represent the phosphates; the numbers in circles are the mean charge neutralization fraction of the tightly bound ions; the shaded circles represent the ion-binding phosphates for the most probable mode (with highest probability p_M). Here, the divalent ion concentration is 0.01 M.

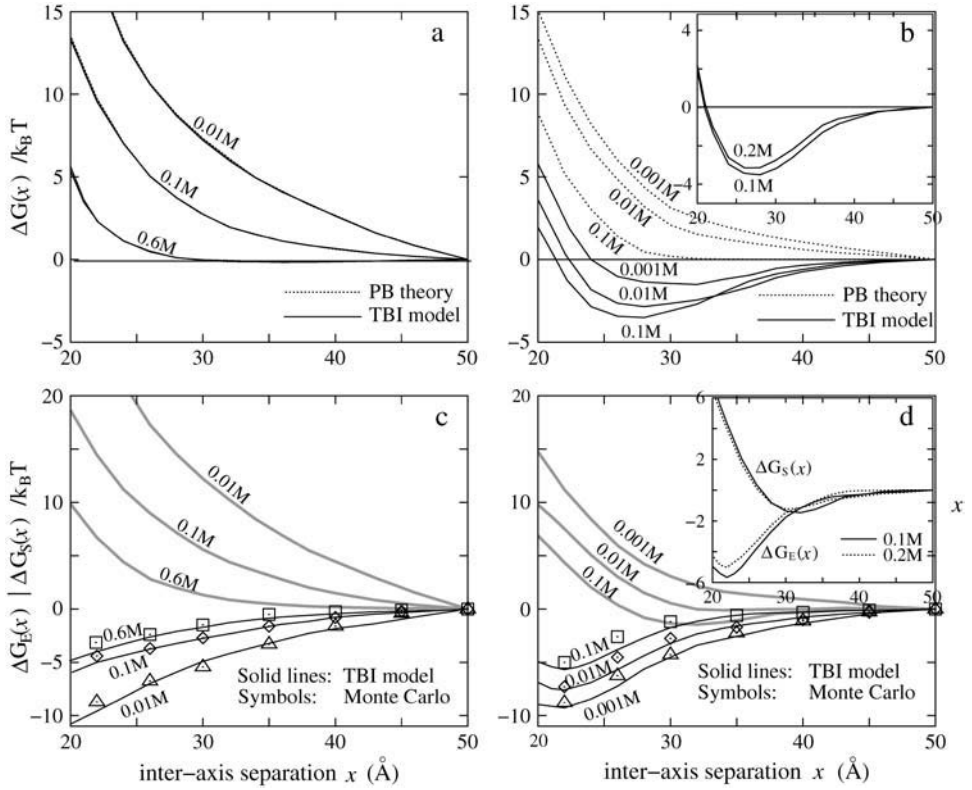

FIGURE 4 (*a*) The free energy $\Delta G(x)$ as a function of interhelix separation x for different monovalent salt concentrations: 0.01 M, 0.1 M, and 0.6 M (from *top* to *bottom*). (*Dotted lines*) Poisson-Boltzmann theory. (*Solid lines*) TBI theory. Some parts of the dotted lines are not visible because they are underneath the solid lines. (*b*) The electrostatic free energy $\Delta G(x)$ as a function of interhelix separation x for different divalent salt concentrations: 0.001 M, 0.01 M, and 0.1 M (from *top* to *bottom*). (*Dotted lines*) Poisson-Boltzmann theory. (*Solid lines*) TBI theory. The inset shows $\Delta G(x)$ at high divalent salt concentration. (*c*) The electrostatic energy $\Delta G_E(x)$ (*solid lines*) and entropic free energy $\Delta G_S(x)$ (*shaded lines*) for different monovalent salt concentrations. (*d*) The electrostatic energy $\Delta G_E(x)$ and entropic free energy $\Delta G_S(x)$ for different divalent salt concentrations. The inset shows $\Delta G_E(x)$ and $\Delta G_S(x)$ at high divalent salt concentrations. The minimum contact distance for parallel helices is $\sim x \simeq 20$ Å.

For the enthalpic free energy $\Delta G_E(x)$, as discussed above, the (correlated) bound cations between the helices would self-organize and interact more strongly with the two negatively charged helices, which lead to a decrease in the electrostatic energy $\Delta G_E(x)$. For smaller x, $\Delta G_E(x)$ decreases more rapidly with x due to the large number of the bound ions between the helices and the smaller distance between the cations and the negatively charged phosphates. However, for very small helix-helix distance ($x \lesssim 23$ Å) when helices are tightly packed, the volume exclusion between the bound ions and helices causes a slight increase in $\Delta G_E(x)$. In fact, when the helices are very closely packed, a fraction of bound ions may be pushed out from the strongly correlated interhelix region due to the volume exclusion and the ion-ion electrostatic repulsion.

From Fig. 4, *c* and *d*, we find that the TBI theory gives good agreement with the Monte Carlo simulations for $\Delta G_E(x)$ (see Appendix D for the details on the Monte Carlo simulations). The competition between $\Delta G_E(x)$ and $\Delta G_S(x)$ results in the free energy landscape $\Delta G(x) = \Delta G_E(x) + \Delta G_S(x)$. From Fig. 4, we find the following distinctive features for the free energies of the system in monovalent and divalent ion solutions:

1. Because the (bound) divalent ions carry higher charges, for small x, the decrease in the electrostatic energy $\Delta G_E(x)$ for divalent ions is more pronounced than for monovalent ions, i.e., as two helices approach each other, $\Delta G_E(x)$ decreases faster in divalent ion solution than in monovalent ion solution.
2. The divalent ions, which carry higher charges, are more efficient in charge neutralization than monovalent ions. As a result, $\Delta G_S(x)$ for divalent ions is much smaller than for monovalent ions, i.e., charge neutralization of the helix requires less divalent ions than monovalent ions. Consequently, as the helices approach each other, divalent ions have a smaller entropic decrease (i.e., smaller free energy $\Delta G_S(x)$ increase) than monovalent ions.
3. The competition between $\Delta G_E(x)$ and $\Delta G_S(x)$ results in an apparent attractive force that tends to bring the two helices together in divalent ion solution in order to lower the free energy. However, in monovalent ion solution, no such attractive force exists, even for high salt concentrations. We note that the analysis here is also in qualitative accordance with the previous simulations for two like-charged spheres in monovalent and divalent salts (64,65).

Ion concentration effect on helix-helix interaction

Fig. 4, *a* and *b*, shows that the ion concentration has great influence on the helix-helix electrostatic interactions. We use c to denote the ion concentration. For monovalent ions, the increase of c significantly weakens the repulsion between DNA helices (see Fig. 4 *a*). This is because higher c gives lower entropic cost for ion-binding and hence more bound ions. A larger number of bounds ions means stronger ionic screening (neutralization) for the helices and thus weaker helix-helix repulsion.

For divalent ions, the relationship between $\Delta G(x)$ and c is more complicated (see Fig. 4 *b*). As the divalent ion concentration c is increased, the attraction between the helices becomes stronger. However, as c continues to increase and exceeds a certain critical value c^*, further addition of salt ions would weaken the attraction. For two helices of 10-bp in divalent ion solution, we find that $c^* \sim 0.1$ M. The salt-enhanced attraction at low c and the salt-weakened attraction at high c may correspond to the salt-induced bundle formation and bundle resolubilization for DNA helices (36,37,93) and for other polyelectrolyte molecules (43–47).

Also shown in Fig. 5 are the minimum free energy $\Delta G_{\min}$, the stable interhelix separation $x_{\min}$, and the mean equilibrium helix-helix distance $\bar{x}$ computed as

$$\bar{x} = \frac{\sum x\, e^{-\Delta G(x)/k_B T}}{\sum e^{-\Delta G(x)/k_B T}},$$

as functions of divalent salt concentration c. We find that $\Delta G_{\min}$, $x_{\min}$, and $\bar{x}$ all show nonmonotonic behavior: to decrease with the increase of c ($<c^*$), and to slightly increase with the addition of salt when c exceeds a critical value c^*. The predicted stable helix-helix separation $x_{\min}$ shown in Fig. 5 as well as the salt dependence of $x_{\min}$ agree with the experimentally measured results for the interhelical spacing of an hexagonal DNA array (36,93,97) (details in Comparisons with Experimental Measurements).

To understand the salt concentration c-dependence shown in Fig. 4 *b*, we further examine the electrostatic energy $\Delta G_E(x)$ and the entropic free energy $\Delta G_S(x)$. As shown in Fig. 4 *d*, with the increase of the (divalent) salt concentration c, the electrostatic energy $\Delta G_E(x)$ increases monotonically, while $\Delta G_S(x)$ decreases significantly for $c < c^*$ but the trend of decreasing stops for $c > c^*$. In the following, we analyze the microscopic mechanisms for such intriguing behaviors of $\Delta G_S(x)$ and $\Delta G_E(x)$. Our motivation here is to distinguish whether the helix-helix attraction is enthalpically driven or entropically driven, and how the different parts of the entropy play different roles in the process.

The entropic free energy $\Delta G_S(x)$

For higher ion concentration c, because of the lower entropic cost for ion-binding, more ions are bound to the helices and the charge neutralization is stronger. Therefore, as the two helices approach each other (i.e., x becomes smaller), the increase in the strength of the negative electric field (around the helices) and hence, the increase in the number of bound ions, are less pronounced for higher c. Consequently, the decrease of the entropy (and the increase of the entropic free energy $\Delta G_S(x)$) for smaller x would be less significant for higher c,

$$\Delta G_S(x)_{\text{higher c}} < \Delta G_S(x)_{\text{lower c}} \text{ for } c \lesssim 0.1\,\text{M}. \qquad (20)$$

See Fig. 4 *d* for the divalent ion concentration from 0.001 M to 0.1 M.

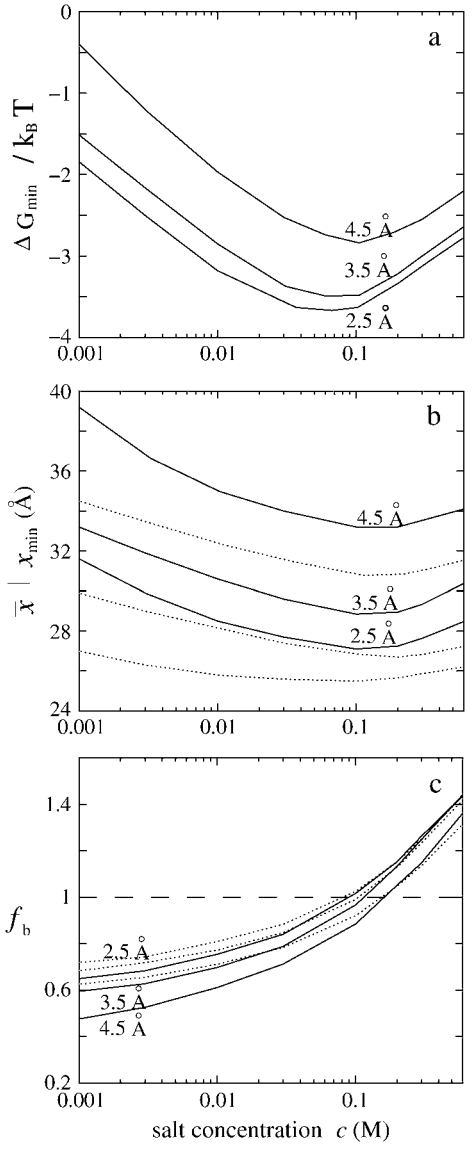

FIGURE 5 (*a*) The minimum free energy $\Delta G_{\min}$ as a function of divalent salt concentration for variant cation radii: 4.5, 3.5, and 2.5 Å (from *top* to *bottom*). (*b*) The equilibrium interhelix separation $\bar{x}$ (*solid lines*) and $x_{\min}$ (*dotted lines*) corresponding to minimum free energy $\Delta G_{\min}$ as functions of divalent salt concentration for different cation radii: 4.5, 3.5, and 2.5 Å (from *top* to *bottom*). (*c*) The mean charge neutralization fraction f_b of the tightly bound ions per phosphate as a function of divalent salt concentration for different cation radii: 4.5, 3.5, and 2.5 Å (from the *top* to *bottom*). The interaxis separations are 50 Å (*solid lines*) and 26 Å (*dotted lines*), respectively.

For very high divalent ion concentration $c \gtrsim 0.1$ M, the ionic entropy decrease upon binding is small and thus more ions would bind to the helices, resulting in possible full-neutralization or over-neutralization (charge inversion); see Figs. 5 and 6. In such cases, as the helices approach each other, the strong Coulomb repulsion between the large number of bound ions causes the ions to avoid each other, especially for the bound ions that reside between helices.

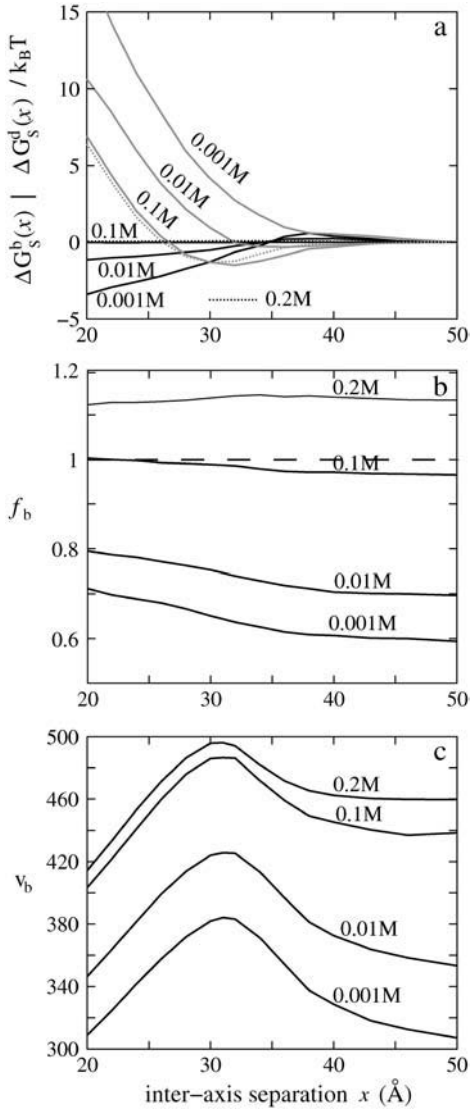

FIGURE 6 (*a*) The entropic free energies $\Delta G_S^d(x)$ of diffusive ions (*black lines*) and the entropic free energy $\Delta G_S^b(x)$ of the tightly bound ions (*shaded lines*) as functions of interhelix separation x for different divalent salt concentrations. (*b*) The mean charge neutralization fraction f_b of the tightly bound ions per phosphate as a function of interhelix separation x for variant divalent salt concentrations. (*c*) The mean volumes v_b (in Å^3) of the tightly bound region per phosphate versus interhelix separation x for different divalent salt concentrations. The minimum contact distance for parallel helices is $\sim x \simeq 20$ Å.

Such effect can cause a saturation in the c-dependence of the number of the bound ions and of the free energy $\Delta G_S(x)$; see Fig. 4 *d* (*inset*). In fact, for the strongly overneutralized case, we find that the amount of the tightly bound ions (especially the tightly bound ions in the interhelix region) slightly decreases when the two helices become closer. Such a prediction is consistent with the results in a recent computer simulation (71).

From the above discussion, we find that as the two helices approach each other, the number of the tightly bound ions (and $\Delta G_S(x)$) would increase for low c and slightly decrease for high c, and the c-dependence is related to charge inversion. This suggests the existence of a critical ion concentration c^* such that $\Delta G_S(x)$ increases with c for $c < c^*$ and decreases slightly for $c > c^*$. From Figs. 4 *d* and 5, we find that $c^* \sim 0.1$ M.

From Fig. 4 *d* (*inset*), we also find that for $c \gtrsim c^*$ and $x \sim 30$–40 Å, $\Delta G_S(x)$ decreases slightly when the two helices are closer, indicating a (slight) entropic attractive force:

$$\Delta G_S(x)\,(\text{smaller}\,x) < \Delta G_S\ (\text{larger}\,x)\ \text{for}\ 30\ \text{Å} \lesssim x \lesssim 40\ \text{Å}\quad \text{and}\ \ c \gtrsim 0.1\ \text{M}. \tag{21}$$

The total entropic free energy $\Delta G_S(x)$ is the net result from the two different types of ions (the tightly bound ions and the diffusive ions). We would like to understand how the different types of ions play different roles in the helix-helix folding process and what results in the slight entropic attraction. In what follows, we examine the component entropic free energies $\Delta G_S^d(x)$ (Eq. 16) of the diffusive ions and $\Delta G_S^b(x)$ (Eq. 17) of the tightly bound ions separately.

Diffusive ions. As shown in Fig. 6 *a*, for low ion concentration $c \lesssim 0.1$ M, as the two helices become closer, $\Delta G_S^d(x)$ of the diffusive ions decreases, resulting in an apparent attractive force between the helices. This is because as the helices approach each other, the aggregation of the phosphate charges causes a stronger cation-attracting field and hence more bound ions (see Fig. 6 *b*) and stronger charge neutralization. As a result, the diffusive ions around the helices are less confined and have larger translational entropy (i.e., lower free energy $\Delta G_S^d(x)$) for smaller x:

$$\Delta G_S^d(x)\,(\text{smaller}\,x) < \Delta G_S^d(x)\,(\text{larger}\,x)\ \text{for}\ c \lesssim 0.1\text{M}. \tag{22}$$

For high salt concentration, the helices are fully or overneutralized. For smaller x, the strong repulsion between the bound ions would inhibit further increase of ion-binding. As a result, the c-dependence of $22\Delta G_S^d(x)$ becomes saturated; see the $\Delta G_S^d(x)$ curves for $c = 0.1$ M and 0.2 M divalent ion concentrations.

Bound ions. The apparent attractive entropic force shown in Eq. 21 can be understood from the entropic free energy $\Delta G_S^b(x)$ for the tightly bound ions. The entropy of the tightly bound ions has two components: the entropy for the partitioning of the different binding modes and the entropy $\sim N_b(x)\Delta S_b(x)$ of the bound ions in tightly bound cells. Here $N_b(x)$ is the number of the bound ions and $\Delta S_b(x) < 0$ is the entropy change for an ion to transfer from the diffusive region into the tightly bound region. The value $\Delta S_b(x)$ is determined by the bulk ion concentration c and the volume v_b of the tightly bound region: $\Delta S_b(x) \sim k_B \ln(v_b(x)c)$.

Fig. 6 *c* shows that as the helices approach each other, the volume of a tightly bound cell $v_b(x)$ varies nonmonotonically: $v_b(x)$ increases for $x \gtrsim 30$ Å and decreases for $x \lesssim 30$ Å. We note that the variation of $v_b(x)$ with x is similar to that of the volume of the condensed ions in CC theory (58–61). The

increase of $v_b(x)$ for $x \gtrsim 30$ Å tends to cause a smaller $|\Delta S_b|$. In contrast, as the helices approach each other, $N_b(x)$ increases, which tends to cause a larger $|\Delta S_b|$ (see Fig. 6 *c*).

For low (divalent) ion concentrations ($c \sim 0.001$–0.01 M in Fig. 6), the $N_b(x)$-effect dominates over the $v_b(x)$-effect, resulting in a net increase of $|\Delta S_b|$ (i.e., an increase in the entropic free energy $\Delta G_S^b(x)$) as x decreases. Therefore, for low ion concentrations, the $\Delta G_S^b(x)$ profile gives no attractive force.

For high (divalent) ion concentrations ($c \sim 0.1$–0.2 M in Fig. 6), as x ($\gtrsim 30$ Å) decreases, the increase in N_b is small (see Fig. 6 *b*) and the $v_b(x)$-effect dominates. As a result, $|\Delta S_b|$ decreases (i.e., $\Delta G_S^b(x)$ decreases) with x, causing an apparent effective entropic attractive force (58); see Fig. 4 *d*, *inset*, and Eq. 21. However, we note that, as we show in the following section, the above entropic effect is weaker than the effect from the electrostatic energy $\Delta G_E(x)$.

The electrostatic energy $\Delta G_E(x)$

As shown in Fig. 4, *b* and *d*, $\Delta G_E(x)$ increases with increased ion concentration c:

$$\Delta G_E(x)_{\text{higher c}} > \Delta G_E(x)_{\text{lower c}}. \tag{23}$$

The salt dependence of electrostatic energy $\Delta G_E(x)$ is a result of the competition between the ion-helix attraction and the ion-ion repulsion. For higher ion concentration, the helices are strongly neutralized (due to more bound ions). For example, the tightly bound ions neutralize ~97% and 70% phosphates in 0.1 M and 0.01 M divalent solutions, respectively, for two separated helices. The strong ion-helix attraction dominates the electrostatic energy $\Delta G_E(x)$.

In a high-c solution, the helices are already significantly neutralized before they approach each other. Therefore, as the two helices become closer, the increase in N_b in a low-concentration c solution is much more pronounced than that in a high-c solution. Consequently, the enhancement in the ion-helix attraction is much more significant for a low c solution. Moreover, in a high-c solution, when the helices, bound by a large number of tightly bound ions, approach each other (e.g., for $x \sim 20$–30 Å), the Coulomb repulsion between the bound ions would further damp the interhelix attraction. Such effect is particularly strong for the overneutralized case. As a result, $\Delta G_E(x)$ is higher for higher ion concentration.

The total free energy $\Delta G(x)$

The combination of $\Delta G_E(x)$ and $\Delta G_S(x)$ gives the total free energy $\Delta G(x) = \Delta G_E(x) + \Delta G_S(x)$. For the divalent ions, from the folding energy landscape $\Delta G(x)$ shown in Fig. 4 *c*, we find that there exists a critical ion concentration c^* (~0.1 M for the two-helix system), which is related to the charge overneutralization as shown in Fig. 5. A higher ion concentration c would strengthen (weaken) the interhelix attraction to stabilize (destabilize) the two-helix system for $c < c^*$ ($c < c^*$). The TBI theory shows that the full-neutralization by the multivalent ions is the starting point of the weakening of the helix-helix attraction. This is in accordance with the previous experimental measurements (43,93), theoretical predictions (94), and computer simulations (71).

In our TBI theory, the ions are assumed to have the charges of bare ions (i.e., completely dissociated ions in solution). Based on this assumption, the charge inversion occurs (83) and may be responsible for the weakening of ion-mediated helix-helix attraction at high concentration. As a caveat, we note that the charge inversion for a polyanion may be accompanied by the association of the co-ions (chloride ions) around the bound cations. Thus, a clearcut boundary for the charge inversion may not exist (37,47). Recently, a different possible mechanism for the resolubilization of DNA bundles has been proposed (93,95): at high concentration, multivalent ions cannot dissociate completely from the co-ions (chloride ions), thus the clusters of the multivalent ions with the associated chloride ions would carry less charges than bare ions. As a result, ions would become less effective to mediate the helix-helix attraction and thus helix-helix attraction is weaker.

Ion size effect on helix-helix attraction

Several experiments have demonstrated the important role of ion size in RNA collapse transition (22), DNA condensation (39), and the compaction of other polyelectrolyte molecules such as anionic rodlike M13 and fd viruses (44,45). In this section, we focus on the physical mechanism and quantitative prediction for the ion size effect. To be specific, we use different ion radii 2.5 Å, 3.5 Å, and 4.5 Å. As shown in Fig. 7 *a*, for small ion radius, the TBI theory predicts a smaller distance (x_{min} and $\bar{x}$) between the helices, a lower minimum free energy (ΔG_{min}), and a stronger helix-helix attraction. In what follows, we discuss the ion size-dependence of the free energy landscape $\Delta G(x)$.

Smaller ions can make closer contacts with the phosphate charges. Such stronger cation-phosphate interaction would stabilize the tightly bound ions, causing a stronger charge neutralization for the polyanionic helices; see Fig. 7 *c*. For example, at $c = 0.01$ M divalent ion concentration, the tightly bound ions with radii 2.5 Å and 4.5 Å neutralize ~75% and 60% phosphate charges, respectively. Therefore, in a solution of small ions, helices are highly neutralized. As the helices approach each other, the increase in the number N_b of the tightly bound ions and the resultant decrease (increase) in the electrostatic energy (entropy) $\Delta G_E(x)$ ($\Delta G_S(x)$) are smaller than in a solution of larger ions (see Fig. 7 *b*):

$$\begin{aligned} 0 &> \Delta G_E(x)_{\text{smaller ion}} > \Delta G_E(x)_{\text{larger ion}}; \\ 0 &< \Delta G_S(x)_{\text{smaller ion}} < \Delta G_S(x)_{\text{larger ion}}. \end{aligned} \tag{24}$$

In addition, Fig. 7 *b* shows that for small x ($\lesssim 23$ Å), $\Delta G_E(x)$ increases rapidly with a decreasing x. This is because

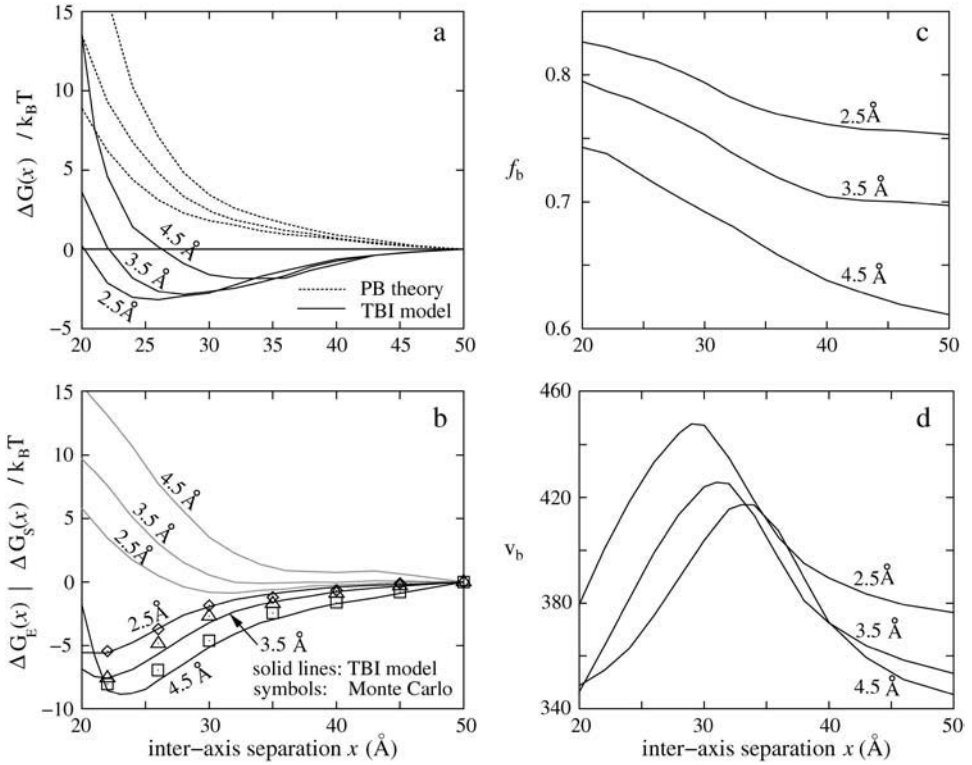

FIGURE 7 (*a*) The free energy $\Delta G(x)$ as a function of interhelix separation x for different divalent ion radii: 4.5 Å, 3.5 Å, and 2.5 Å (from *top* to *bottom*). The divalent salt concentration is 0.01 M. (*Dotted lines*) Poisson-Boltzmann theory. (*Solid lines*) TBI theory. (*b*) The electrostatic energy $\Delta G_E(x)$ (*solid lines*) and entropic free energy $\Delta G_S(x)$ (*shaded lines*) for different divalent ion radii. The divalent salt concentration is 0.01 M. (*Solid lines*) TBI theory. (*Symbols*) Monte Carlo simulations. (*c*) The mean charge neutralization fraction f_b of the tightly bound ions per phosphate as a function of interhelix separation x for different cation sizes. (*d*) The mean volume v_b (in Å^3) of the tightly bound regions per phosphate as a function of interhelix separation x for different divalent cation sizes. The minimum contact distance for parallel helices is $\sim x \simeq 20$ Å.

the bound ions are pushed out from the strongly correlated interhelix region when the helices are very close. Such effect is stronger for more bulky ions because of the larger excluded volume, as shown in Fig. 7 *b*.

In Eq. 24, the ion size effect is stronger for the entropic $\Delta G_S(x)$ than for the enthalpic $\Delta G_E(x)$, and the net free energy $\Delta G(x) = \Delta G_S(x) + \Delta G_E(x)$ gives a stronger decrease for smaller ions (see Fig. 7 *a*):

$$\Delta G(x)_{\text{smaller ion}} < \Delta G(x)_{\text{larger ion}}. \tag{25}$$

As a result, the helices are more stabilized by smaller ions.

Moreover, because smaller ions can make closer contact with the helices, the helices can be more closely packed at a smaller stable distance, causing a smaller interhelix distance and lower free-energy minimum (see Figs. 7 *a* and 8, *a* and *b*):

$$(x_{\min})_{\text{smaller ion}} < (x_{\min})_{\text{larger ion}};$$
$$(\Delta G_{\min})_{\text{smaller ion}} < (\Delta G_{\min})_{\text{larger ion}}.$$

The above results show that smaller ions are much more effective in inducing helix-helix compaction and the resultant helix-helix complex is much more compact.

The above results are in accordance with the recent experiments (22,39,44,45). The sensitivity of ΔG_m and $x_{\min}$ (or $\bar{x}$) on the ionic radius might also (partially) account for the experimental finding that some divalent ions can condense DNA molecules whereas other divalent ions cannot. For example, at room temperature and in aqueous solution, Mg^{2+} ions cannot condense DNA, while Cu^{2+} ions can induce DNA condensation (30,34,96–99). Mg^{2+} ions have large hydrated radii (~4.5 Å) (83,84,100), thus the ion-mediated attraction is not strong and the stable helix-helix distance is not small enough to form a compact helix-helix collapsed structure. Another possible reason for the different abilities of different divalent ions in condensing DNA is the site-specific ion binding. For example, Mg^{2+} ions bind to phosphate groups, while Mn^{2+}, Cu^{2+} ions bind to both phosphate groups and bases (1,98,99). The binding of ions to bases may favor condensed DNA because of the stronger helix-helix attraction due to the specific charge distribution on the helix surface (77,101) and the stronger flexibility for helix bending (98,99,102,103). The TBI model allows the bound ions to move around the phosphates and inside the grooves (83,84). However, the model does not treat the site-specific ion-binding.

The present TBI model does not treat the possible ion desolvation upon binding. In the folding of nucleic acid molecules, the polyanionic chain can fold into compact structures, some of which can form electrostatically attractive pockets for ion binding (6,10). In these pocket regions and in regions with ions bound to specific charged groups, ions can be desolvated. A dehydrated ion can have a much smaller size than a hydrated one. For example, the radius of a Mg^{2+} ion can change from 4.5 Å (hydrated) to 0.65 Å (fully dehydrated) in the dehydration process (6,83,84,100). The (small) dehydrated cations can approach the surrounding negatively charged groups at a much smaller distance and the interaction is much stronger.

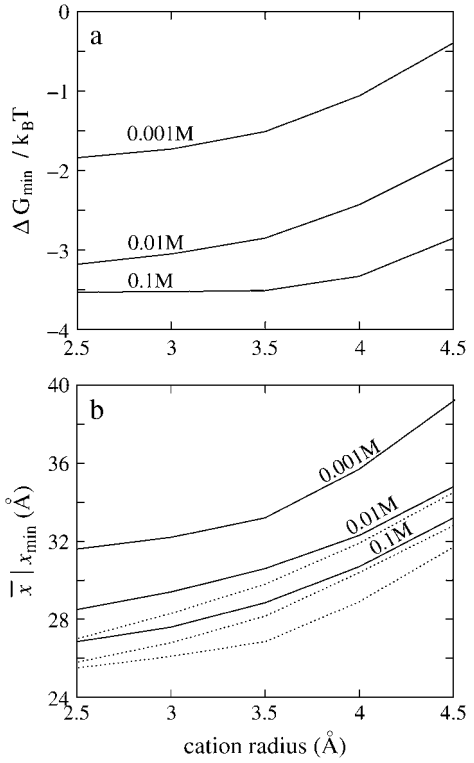

FIGURE 8 (*a*) The minimum free energy ΔG_{min} versus divalent ion radius for different divalent salt concentrations: 1 mM, 10 mM, and 100 mM (from *top* to *bottom*); (*b*) The equilibrium interhelix separation $\bar{x}$ (*solid lines*) and x_{min} (*dotted lines*) corresponding to minimum free energy ΔG_{min} as a function of cation radius for different divalent salt concentrations: 1 mM, 10 mM, and 100 mM (from *top* to *bottom*).

In addition, the dielectric effects (e.g., the dielectric discontinuity (83,102) and the dielectric saturation (104)) result in a stronger charge-charge interaction owing to the decreased effective dielectric constant (83,102,104,105) (as compared to the dielectric constant bulk solvent). To account for the dielectric effect, the distance-dependent dielectric constant $\epsilon(\mathbf{r})$ has been introduced (104,105). The use of $\epsilon(\mathbf{r})$ can cause a stronger charge-charge interaction, especially between the nearby charges, and a stronger ion-ion correlation and helix-helix attraction.

The dehydration and the dielectric effects are intrinsically related to each other (6). The distance-dependent dielectric constant tends to lower the electrostatic free energy and to compensate the electrostatic penalty due to possible dehydration in the binding process. So a distance-dependent dielectric constant may favor the dehydration of the bound ions. Further development of the model would include both the ion desolvation and the dielectric effect.

Dielectric constant dependence of helix-helix attraction

Various experiments have demonstrated the important role of the dielectric property of solvent in DNA condensation (31,35,96,106,107). For example, experiments have shown that the addition of methanol in solvent favors the ion-mediated DNA condensation and aggregations (31,35,96). In this section, to be specific, we study the cases with dielectric constant ϵ of solvent equal to 70, 78 (= dielectric constant of aqueous solvent at 25°C), and 90. In Fig. 9 *a*, we show the free energy landscape $\Delta G(x)$ predicted from the TBI theory as a function of interhelix distance x for different dielectric constants. From the $\Delta G(x)$ profile, we find that the decrease of dielectric constant enhances the attraction between the two helices.

The relationship between the helix-helix attraction and ϵ can be understood as follows. The decrease of ϵ weakens the dielectric screening of the solvent and thus strengthens the charge-charge interaction, including the ion-helix binding. As a result, smaller ϵ leads to more bound ions and stronger charge neutralization of the helix. For example, in a 0.01 M divalent ion solution, the bound ions neutralize ~82% and 52% phosphate charges in $\epsilon = 70$ and $\epsilon = 90$ solvents, respectively (see Fig. 9 *c*).

When the helices approach each other in a low-ϵ solvent, owing to strong charge neutralization of the helices, the increase in the amount of the tightly bound ions is small, resulting in a smaller increase in the entropic free energy $\Delta G_S(x)$ and a smaller decrease in the electrostatic energy $\Delta G_E(x)$. Since $\Delta G_S(x)$ shows a stronger ϵ-dependence than $\Delta G_E(x)$ (see Fig. 9 *b*), the total free energy $\Delta G(x) = \Delta G_S(x) + \Delta G_E(x)$ is lower (more negative) for smaller ϵ, i.e., the helices have a stronger tendency to approach each other.

The above predictions from the TBI theory are in accordance with the experimental observations (31,35,96,106,107). In the experiments, the addition of methanol, alcohol, and urea may influence not only the dielectric constant (the polarization of solvent molecules), but also the ion-binding specificity (hydrogen-bond mediated ion-nucleic acid interaction). The ion binding specificity may play a role in the helix-helix interaction.

Length effect on helix-helix attraction

Fig. 10 *a* shows that for helix length $N = 6$–12 bp (of each helix) and $x \gtrsim 25$ Å, the two-helix system has lower free energy $\Delta G(x)$ for longer helices. Fig. 10 *b* shows that the minimum free energy Δg_{min} (= $\Delta G_{min}/N$) per basepair and the equilibrium interhelix distance $\bar{x}$ decreases with length N before saturation occurs for $N \gtrsim 10$ bp.

For large N, the electric field near the helix surface is stronger, causing more ions to bind to helices and a lower free-energy minimum $\Delta G_{min} = N\ \Delta g_{min}$. On the other hand, a larger number of bound ions means a stronger charge neutralization, which causes Δg_{min} to become saturated for larger N. Therefore, as shown in Fig. 10 *b*, the equilibrium interhelix distance $\bar{x}$ would decrease with increasing N and then approaches a constant for $N \gtrsim 10$ bp. In contrast, from Fig. 10 *a*, the most stable interhelix separation x_{min} (that gives ΔG_{min}) keeps nearly invariant (~28 Å) for different N. The saturation of Δg_{min} and $\bar{x}$ for $N \gtrsim 10$ bp and the weak

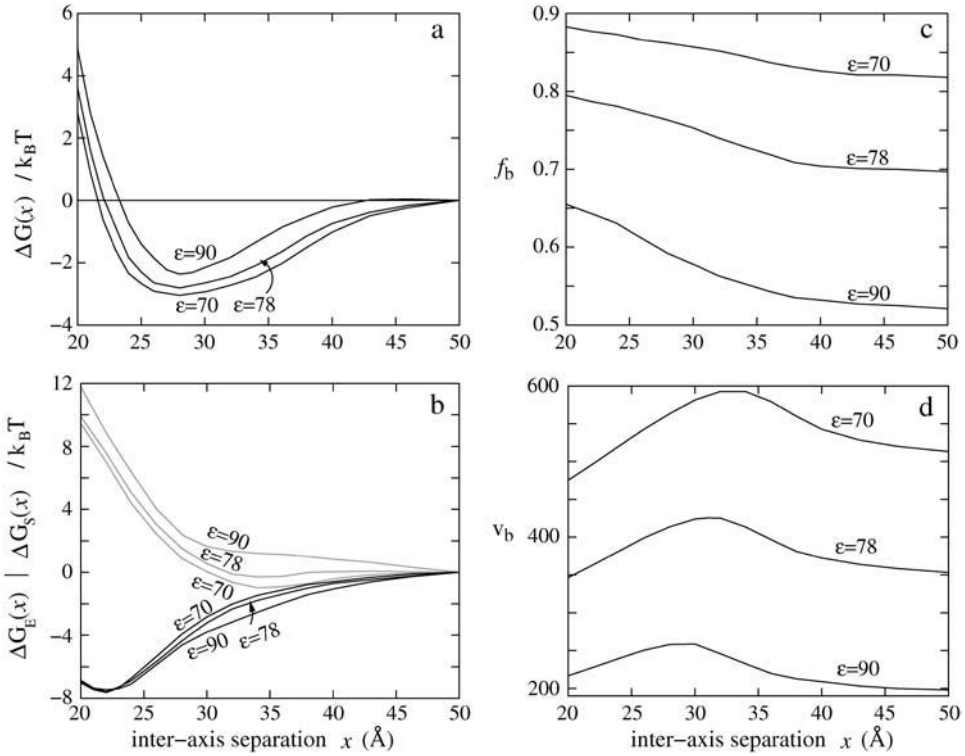

FIGURE 9 (*a*) The free energy $\Delta G(x)$, calculated from the TBI theory, as a function of interhelix separation x for different solvent dielectric constants ϵ: 90, 78, and 70 (from *top* to *bottom*). (*b*) The electrostatic energy $\Delta G_E(x)$ (*solid lines*) and entropic free energy $\Delta G_S(x)$ (*shaded lines*) for different solvent dielectric constant ϵ. (*c*) The mean charge neutralization fraction f_b of the tightly bound ions per phosphate as a function of interhelix separation x for different solvent dielectric constants. (*d*) The mean volume v_b (in Å^3) of the tightly bound regions per phosphate as a function of interhelix separation x for different solvent dielectric constants. The divalent salt concentration is 0.01 M. The minimum contact distance for parallel helices is $\sim x \simeq 20$ Å.

N-dependence of x_{min} suggest that the predicted results for finite helices may be applicable to experiments for longer helices.

Computational and experimental studies have been performed to investigate the helix length-dependence for helix-ion electrostatic interactions. It was found that the length-dependence (helix end effect) can be extended to larger lengths, especially in low (Na^+) salt (108–110). The helix length-dependence in a divalent solution is weaker than in a Na^+ solution because of the much stronger ion binding and charge neutralization. In the present TBI model for the two-helix system, due to the exponentially increasing number of the possible ion binding modes, the partition function calculation for long helices is computationally demanding. Nevertheless, our calculations for the short helices are able to show the length-dependence and the asymptotic saturation effect of the length-dependence.

Comparisons with experimental measurements

Since experimental measurement for the folding energy landscape $\Delta G(x)$ and the force for the helix-helix system is difficult, direct quantitative theory-experiment comparisons on the folding energy landscape are not currently available. Nevertheless, for DNA array (DNA aggregates), the osmotic pressures have been measured experimentally by the osmotic stress technique (96,97,111,112). In this section, based on the pairwise DNA helix-helix interactions, we calculate the osmotic pressure and compare the results with the experimental data. For an hexagonal DNA array (59,62,101,111,112) (see Fig. 11 *a*), the mean free energy $\Delta g(x)$ per molecule, shown in the shaded hexagon formed by the dashed lines in Fig. 11 *a*, can be approximately calculated through the summation over the pairwise helix-helix interactions between nearest-neighbor pairs (59,101,111–113),

$$\Delta g(x) = \sum_{i=1}^{6} \Delta G_i(x)/2, \tag{26}$$

where $\sum_{i=1}^{6} \Delta G_i(x)$ is the total free energy between an helix and its six neighbors and the factor 1/2 is used to remove double-counting. The value ΔG_i is the free energy for the two-helix system of a helix and its i^{th} neighbor. Here we have neglected the nonadditive effect in multiple helix packing and kept only interactions between the nearest-neighboring helices (59,101,111–113), i.e., when computing the interaction between two helices, we ignore the existence of other helices.

The osmotic pressure $\Pi(x)$ as a function of the helix-helix distance x can be calculated from (62,101,111,112)

$$\Pi(x) = -\frac{\partial \Delta g(x)}{\partial V}, \tag{27}$$

where $V = L \times A$ is the volume of the hexagonal region around each helix, L is the length of each helix ($L = 3.4\ N$ for B-DNA helix), and $A = \sqrt{3}x^2/2$ is the average cross section area per molecule in the DNA array (the area of the *shaded hexagon* in Fig. 11 *a*).

Ion valency and ion concentration dependence of the osmotic pressure

Fig. 11 *b* shows the relationship between the osmotic pressure and the interhelix separation for $MnCl_2$ and NaCl

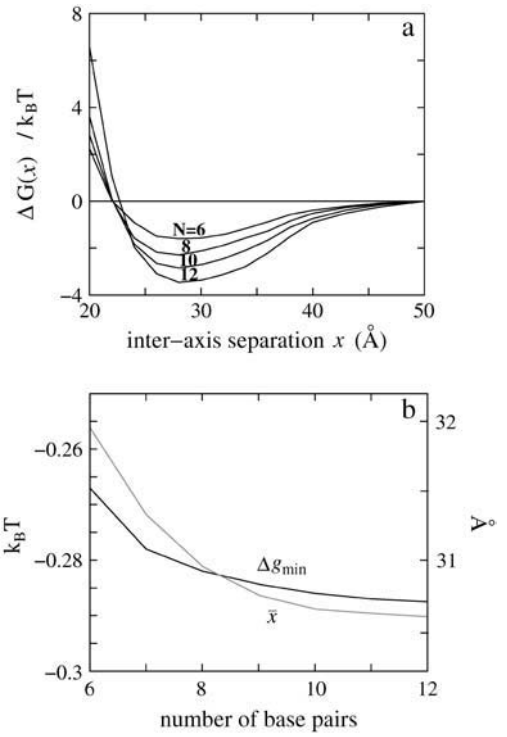

FIGURE 10 (*a*) The free energy $\Delta G(x)$, calculated from the TBI theory, as a function of interhelix separation x for different DNA helical lengths: 6, 8, 10, and 12 bp (from *top* to *bottom*). The divalent salt concentration is 0.01 M. The value $\sim x \simeq 20$ Å is the minimum contact for parallel helices. (*b*) The minimum electrostatic free energy per basepair $\Delta g_{\min}$ ($= \Delta G_{\min}/N$; *left y-axis*) and the equilibrium interhelix separation $\bar{x}$ (*right y-axis*), calculated from the TBI theory, as functions of DNA length (basepair) per helix.

solutions. In the calculation, we use 3.5 Å for the radii of Na^+ (83,84). For Mn^{2+}, we use 3.5 Å. The smaller radius of Mn^{2+} than Mg^{2+} (~4.5 Å (83,84,100)) may effectively account for Mn^{2+}'s stronger binding affinity to nucleic acids (100,114) than Mg^{2+}. Fig. 11 *b* shows that the predictions from the TBI theory agree with the experimental measurements (96,111). For NaCl, the interhelix interaction is repulsive, while for $MnCl_2$, the ion-mediated interaction is attractive (97). Fig. 11 *b* also shows the salt-concentration effect on the osmotic pressure. For NaCl, the increase of salt concentration enhances ion binding (charge neutralization) as well as ionic screening, which causes a reduction in the interhelix repulsion (111,112). For $MnCl_2$, the increase of salt concentration reduces the entropic cost for ion-binding. The self-organization of the bound ions and the lower entropic penalty lead to the stronger overall attraction and shorter helix-helix distance, as discussed above.

Ion size dependence of the osmotic pressure

Fig. 11 *c* shows the osmotic pressure as functions of the interhelix separation for divalent ions with different radii. We use 3.5, 4.3, and 4.5 Å for the ion radii of Mn^{2+}, Ca^{2+}, and Putrescine^{2+} (100,114), respectively. The TBI predictions agree with the experimental data for different divalent ions. Smaller divalent ions result in a stronger attraction and closer stable helix-helix distance. This can be attributed to the stronger electrostatic ion-DNA attraction and the smaller excluded volume effect. Experiments found no measurable helix-helix attraction for Ca^{2+} and Putrescine^{2+}, while the TBI theory predicts a weak attraction. Such theory-experiment difference might be due to the site-specific ion-binding that has been ignored in the TBI theory.

Temperature dependence of the osmotic pressure

The osmotic pressures of the DNA aggregates in $MnCl_2$ are plotted as functions of the interhelix separation for different temperatures in Fig. 11 *d*. As we discussed in the previous sections, in accordance with the experimental findings (97,101,99,115), the TBI theory predicts that for a higher temperature, helix-helix attraction become stronger, because the dielectric constant of solvent is smaller (see Eq. 30). As a result, with the decreasing x, the osmotic pressure rises more steeply for higher temperature.

The differences between the experimental measurements and theoretical predictions may come from the following reasons: 1), The calculation of osmotic pressure assumes the additivity of the pairwise helix-helix interactions and includes only the interactions between the nearest-neighboring helices. 2), The theory cannot treat the possible site-specific ion binding that might play a role in the experiments. 3), The calculation is based on helices of 10 bp, which are much shorter than the helices in experiments. 4), The theory cannot treat the hydration effects, which, as suggested in experiments, may play an important role (96,97).

CONCLUSIONS AND DISCUSSION

The tightly bound ion theory can treat the correlations and the fluctuations for the bound ions (83). The theory has been validated by extensive comparisons not only with computer (Monte Carlo) simulations and the PB and CC theories (83), but also with helix-coil transition experiments for both Na^+ and Mg^{2+} ion solutions (84). In this study, based on the TBI theory, we calculate the electrostatic free energy landscape $\Delta G(x)$ for a system of two parallel DNA helices and analyze the driving force for the ion-mediated helix-helix attraction. We then investigate how the ion valency, ion concentration, ion size, and solvent dielectric constant influence the free energy landscape $\Delta G(x)$ and the force between the helices. Our predictions agree with the available experiments and the Monte Carlo simulations. The following is a brief summary of our major findings:

1. The ion-mediated helix-helix attraction results from the decrease in electrostatic energy $\Delta G_E(x)$ due to the self-organization of the bound ions between the helices, and the entropic effect $\Delta G_S(x)$ opposes the close approach

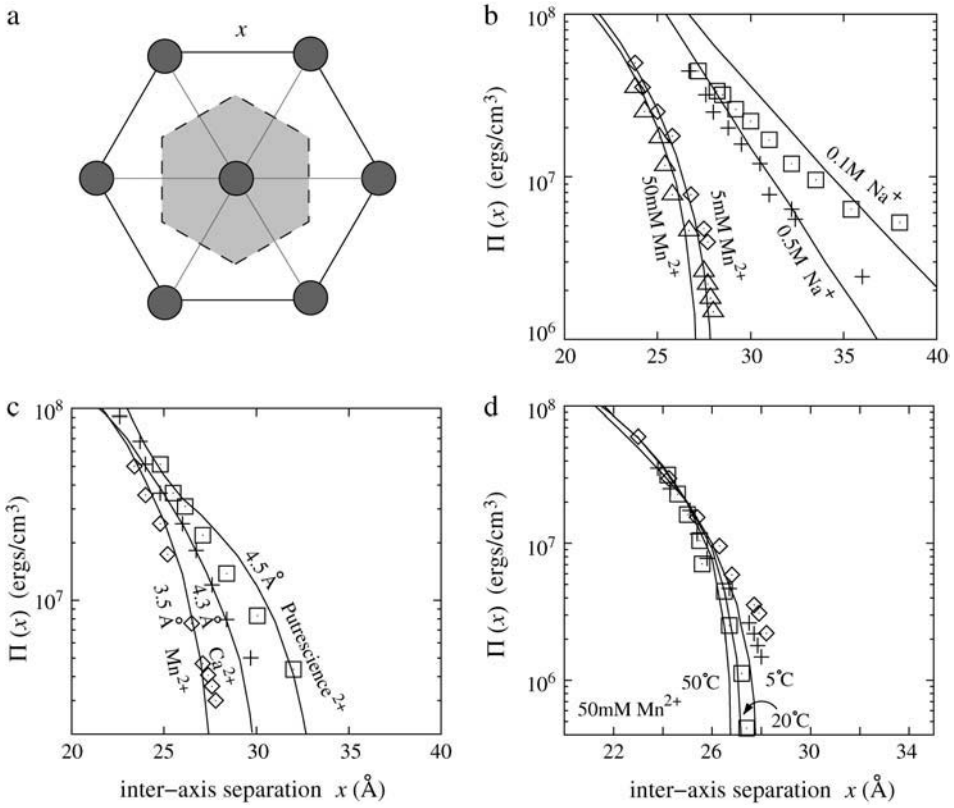

FIGURE 11 (*a*) Illustration for hexagonally ordered DNA array (from *top view*). The shaded circles represent the DNA helices, and the hexagonal area denoted by light shading is the cross area per molecule. (*b*) The osmotic pressures of DNA array as functions of interhelix separation x for different NaCl and $MnCl_2$ concentrations. Symbols are experimental data: ◇, 5 mM $MnCl_2$ (97); △, 50 mM $MnCl_2$ (97); □, 0.1 M NaCl (111); and +, 0.5 M NaCl (111). Solid lines are calculated from the TBI theory together with the use of Eq. 27. The temperature is at 20°C. (*c*) The osmotic pressures for divalent ions with different radii: 3.5 Å, 4.3 Å, and 4.5 Å (from *left* to *right*). Symbols are experimental data: ◇, 10 mM $MnCl_2$ (97); +, 10 mM $CaCl_2$ (97); and □, 10 mM Putrescine Cl_2 (97). Solid lines are calculated from the TBI theory and with Eq. 27. The temperature is at 20°C. (*d*) The osmotic pressures for 50 mM $MnCl_2$ at different bath temperatures: 5°C, 20°C, and 50°C (from *left* to *right*). Symbols are experimental data: ◇, 5°C (97); +, 20°C (97); and □, 50°C (97). Solid lines are calculated from the TBI theory with the use of Eq. 27. The minimum contact distance for parallel helices is $\sim x \simeq 20$ Å.

between the helices. Ion valency, ion concentration, ion size, and solvent dielectric constant can affect the competition between energy and entropy, which determines the overall helix-helix interaction.

2. For monovalent ions, both the PB and the TBI theories predict the repulsive interaction between two helices. For divalent ions, the TBI theory, which accounts for the correlations, predicts an effective attraction between the helices, while the PB theory predicts the helix-helix repulsion only. The TBI theory predicts that, depending on the ion concentration, two 10-bp helices in divalent ion solutions can be stabilized at a distance of 26–35 Å and the interhelix attractive force can reach $-0.37\ k_BT$/bp for small divalent ions.
3. Ion concentration c plays an important role in the ion-mediated attraction between DNA helices. In a divalent ion solution, interhelix attraction is stronger for higher ion concentration but decreases (slightly) when the ion concentration becomes very high ($c > c^* = 0.1$ M for two 10-bp helices in a divalent ion solution). Correspondingly, the equilibrium helix-helix distance decreases with the increase of ion concentration and increases slightly if ion concentration exceeds the critical value c^*.
4. The ion-mediated attraction between DNA helices is dependent on ion size. Smaller ions would induce stronger helix-helix attraction and shorter equilibrium helix-helix distance.
5. The decrease in the dielectric constant would enhance the effective electrostatic helix-helix attraction.
6. The elevation of temperature favors a closer approach between the helices.

Although the present predictions agree with the available experimental measurements and the computer simulations, the theory is based on several simplified approximations. For example, we have neglected the possible deformation of the helices and the partially unfolded states of the helices (84). Moreover, we consider only the parallel helices and neglect configurations with the tilted helices. For the tightly bound ions, we allow them to move in the tightly bound cells (including the grooves), but we do not consider the specific binding between ions and specific groups of the helices. For example, Mg^{2+} ions prefer to bind to DNA phosphate groups, while some other divalent metal ions (e.g., Cu^{2+} and Mn^{2+}) can bind to both phosphates and bases (1,98,99). We have also neglected the possible dehydration effect for bound ions in tightly bound regions (10). In addition, in the calculation of the osmotic pressure, we assume the additivity for the helix-helix interactions and only consider the nearest-neighbor helices in the array (60,101,111–113). Nevertheless, the agreement with experimental measurements suggest that the present predictions are able to provide a physical mechanism for the electrostatic interactions between realistic nucleic acid helices.

The full energy landscape of the two-helix system is determined by the complete ensemble of the two-helix configurations, including the rotated helix-helix configurations. Helix rotation is important for the close packaging of nucleic acid structures (61). Studies (Tan and Chen, 2006, unpublished) on two helices with arbitrary angles suggest a strong angle-dependence of the helix-helix interaction. For high Mg^{2+} concentration, the parallel configuration is most favorable because of the strongest attraction, while for very low Mg^{2+} concentration and for Na^+ solution, configurations with large helix-helix angles (extended configurations) are more favorable in order to achieve the maximum avoidance between the repulsive helices. The parallel and the extended configurations correspond to the strong and weak helix-helix correlations, respectively. A recent computer simulation revealed similar angle-dependence of the helix-helix interaction (71).

The helix-helix interaction is important for DNA condensation and RNA collapse (1,2). The helix-helix attraction mediated by multivalent ($z \geq 2$) ions has been considered to be responsible for the DNA condensation (30–40). RNAs have more complex secondary and tertiary structural segments (e.g., different loops and helices) (1,16–19). Therefore, RNA collapse can be more complicated than DNA condensation (1,20–29,125). The Mg^{2+}-mediated helix-helix attraction indicates that Mg^{2+} is much more efficient than Na^+ in causing the ion-mediated nucleic acid compaction, and Mg^{2+} can induce a more compact state than (high concentration) Na^+ ions. Experimental studies suggest that the tertiary contacts play indispensable roles in the formation of the compact and specific RNA structure (28,29,125). Our study implies that in addition to the specific tertiary interactions and the nonspecific electrostatic screening effect, the helix-helix attraction can also make significant contributions to assist the folding of RNA. Moreover, RNA folding often involves multiple helices. The large number of helices may act cooperatively to further enhance the effect of helix-helix attraction in RNA folding.

APPENDIX A: TREATMENT FOR LONG HELICES

The TBI theory accounts for the discrete binding modes in order to treat the correlations and fluctuations for the bound ions. The tightly bound region is divided into $2N$ tightly bound cells for a N-bp nucleic acid helix, each around a phosphate. The number of the tightly bound ions in each of the $2N$ cells defines a binding mode. For example, if we allow, at most, two (or one) ions in each cell, there would be 3^{2N} (or 2^{2N}) modes for the tightly bound ions. Our previous calculations based on TBI theory have shown that it is appropriate to assume that one tightly bound cell contains, at most, one tightly bound ion for both Na^+ and Mg^{2+} solutions (83,84). This is because for Na^+, there are only very few tightly bound ions, and for Mg^{2+}, one tightly bound ion can change a negatively ($-e$) charged cell into a positively charged one ($+e$), which would inhibit further binding of the (positively charged) cations. Therefore, for an N-bp helix, the number of tightly bound modes can be practically limited to 2^{2N}. For a 10-bp DNA, the number of binding modes is $2^{20} = 1{,}048{,}576$. But for longer nucleic acids, the number of binding modes increases exponentially with the length N; e.g., for a 20-bp DNA, there are $2^{40} \simeq 1 \times 10^{12}$ binding modes, which makes an exhaustive enumeration of all the modes computationally impossible. To circumvent the problem, we have developed an approximate method to simplify the large number of the binding modes in the partition function calculation.

The central idea of the method is to treat the low-probability (high free energy) modes and the high-probability (low free energy) modes separately. For the high-probability binding modes, we treat them rigorously, whereas for the large number of the low-probability modes, we use an approximate random sampling method. As discussed previously (83,84), for a fixed number of tightly bound ions N_b, the difference in the free energy for the different binding modes is dominated by the electrostatic energy G_E^b (Eq. 8) inside the tightly bound region. For each N_b, we identify the high-probability modes as those with low G_E^b.

To reduce the computational complexity of the enumeration for binding modes, for all the possible numbers (N_b', N') such that $N_b' \leq N'$ and $N' \leq N$, we compute the lowest energy for N_b' tightly bound ions residing in N' tightly bound cells. First, we assign N_b' ions to the N' phosphates according to the sequential lowest-energy principle (116). We assign ion 1 to the phosphate with the most negative electric potential; after the assignment of ion-1, recalculate the electric potentials for the rest (empty) of the phosphates and assign ion-2 to the most negative (empty) phosphate. After the assignment of N_b' ions to the N' phosphates, the N_b' ions are allowed to relax on the N' phosphate sites. Every ion can jump to the rest $N' - N_b'$ empty sites (phosphates) with the jumping probability

$$p_i = \frac{\exp(-\Delta E_i/k_BT)}{\sum_i^{N'-N_b'}\exp(-\Delta E_i/k_BT)}, \tag{28}$$

where ΔE_i is the change of the Coulomb energy for jumping to the empty site i. The lowest energy, or one of the lowest energies, can be found in a reasonable computational time because the sampling space is limited. In this way, we can obtain the lowest electrostatic energy E_{min} or one of the lowest energies for different N_b' ions on N' phosphates ($N_b' \leq N' \leq N$). Then we can set a critical value of ΔE_c to separate the low-energy ($G_E^b \leq E_{min} + \Delta E_c$) modes and high-energy ($G_E^b > E_{min} + \Delta E_c$) modes.

In the enumeration of the binding modes for partition function calculation, for each of the low-energy modes, we calculate the partition functions using Eq. 7. For the high-energy modes, we randomly choose a large amount of high-energy modes and calculate their partition functions from Eq. 7. Therefore, the total partition function is given by the summation of the two parts,

$$Z = \sum_{M=1}^{M_l} Z_M + \sum_{M=1}^{M_0} Z_M \times \frac{M_h}{M_0}, \tag{29}$$

where M_l and M_h are the number of the low- and high-energy modes, and M_0 is the number of the high-energy modes that are (randomly) selected. In this way, the thermodynamic properties for the system can be calculated.

Although the above procedure depends on the selections of ΔE_c and M_0, as a control, we have tested the ΔE_c and M_0- dependence and compare the results with the exact mode enumeration for short helix lengths. As shown in Fig. 12, the results are quite robust as tested against the different choices of ΔE_c and M_0.

APPENDIX B: STRUCTURAL MODEL FOR DNA HELIX

We adopt B-DNA as the structural model for DNA since B-DNA is the most common and stable form over a wide range of ionic conditions and sequences (1,117). In this study, a reduced atomic model, the grooved primitive model, is used to model DNA helix (83,84,118); see Fig. 1. The grooved primitive model has been shown to be able to give detailed ion distribution that agrees well with the all-atomic simulations (118). In the grooved model, we represent an N-bp DNA structure as two helical strands, each with N nucleotide units, around a central cylindrical rod of radius $r_{core} = 3.9$ Å. Two hard spheres are used to represent a nucleotide unit. A charged sphere with a point

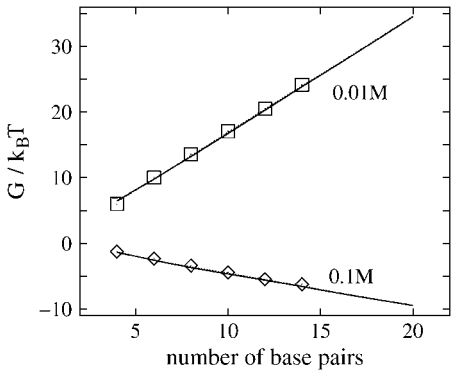

FIGURE 12 The free energy G (Eq. 12), calculated from the TBI theory, versus DNA length $N(-\text{bp})$ for different divalent ion concentrations: 0.01 M and 0.1 M (from *top* to *bottom*). (*Solid lines*) Calculated with the use of Eq. 29; $\Delta E_c = 4\ k_BT$ and $M_0 = 6N^4$. (*Dotted lines*) Calculated with the use of Eq. 29; $\Delta E_c = 3\ k_BT$ and $M_0 = 4N^4$. (*Symbols*) Calculated through the exact enumeration on binding modes.

charge $-e$ (e = proton charge) at the center is used to represent the phosphate group and a electrically neutral sphere is used to represent the rest of the atoms. The phosphate sphere is placed at the center of the phosphate group and the neutral sphere lies between the phosphate sphere and the cylindrical rod. Both spheres have radius of $r_0 = 2.1$Å (118). For the canonical B-DNA, the phosphate charge positions (= the center of the charged sphere) (ρ_i^s, θ_i^s, z_i^s) are given by the following equations (119): $\rho_i^s = 8.9$ (Å); $\theta_i^s = \theta_0^s + i\,36°$; $z_i^s = z_0^s + i\,3.4$ (Å), where $s = 1, 2$ denotes the two strands and $i = 1, 2, \ldots N$ denotes the nucleotides on each strand. The parameters (θ_0^s, z_0^s) for the initial position are (0°, 0Å) for the first strand and (154.4°, 0.78 Å) for the second strand, respectively. For simplicity, the central cylindrical rod in the DNA model is replaced by $N/2$ spheres with radii 4 Å (84). Then a helical basepair is represented by five spheres: one large central sphere, two phosphate spheres, and two neutral spheres, which lie between phosphate spheres and the central big one. The z coordinates of central large spheres are taken to be the averaged z coordinates of the other four spheres (84).

APPENDIX C: PARAMETER SETS AND NUMERICAL DETAILS

In this work, the ions are assumed to be hydrated (83, 84). The radii of the hydrated monovalent and divalent cations used in the calculations are 2.5 Å and 3.5 Å, respectively. The dielectric constant ϵ of the interior of the molecule is set to be 12, which is an experimentally measured value (120), and ϵ of solvent is set as the value of bulk water ($\epsilon = 78$ at 25°C). For a general temperature t (in Celsius), the following empirical formula is used for the solvent dielectric constant ϵ (121),

$$\epsilon(t) = 87.740 - (0.4008)t + (9.398\times10^{-4})t^2 - (1.41\times10^{-6})t^3. \quad (30)$$

Both PB and TBI model require the numerical solution of the nonlinear PB equation. We have developed a three-dimensional algorithm to numerically solve the nonlinear PB equation (83). A thin layer of one cation radius is added to the molecular surface to account for the excluded volume layer (charge-free layer) of cations (10,83,84). We use the three-step focusing process to compute the detailed electrostatic potential near the molecules (48,83,84). The grid size in the first run of the three-focusing process depends on the salt concentration used. Generally, we choose a grid-size six times larger than the Debye length, to effectively include the salt-screening effects in solution. The resolution of the first run varies with the grid size to make the iterative process computationally efficient (83,84). We choose the Cartesian coordinate system with the x axis connecting the two helices. The grid size (L_x, L_y, L_z) in the second and the third runs are kept at (204 Å, 136 Å, 136 Å) and (136 Å, 68 Å, 68 Å), respectively, and the corresponding resolutions are 1.36 Å per grid and 0.68 Å per grid, respectively. As a result, the number of the grid points is $151 \times 101 \times 101$ in the second and $201 \times 101 \times 101$ in the third run. Our control tests for different grid resolutions show robust results.

APPENDIX D: MONTE CARLO SIMULATION

In this work, to validate the predictions of the TBI theory for the two-helix system, with the use of the cell model (83,108), we perform the hybrid Monte Carlo (122–124) to calculate the electrostatic energy for the two helices in salt solution. The hybrid Monte Carlo method has been shown to give the improved sampling, compared with the canonical Monte Carlo method (122–124). In the simulation, to remove (or minimize) the boundary effect, the size of the cell is always kept six times larger than the Debye length of the solution and the interhelix distance between two helices. The numbers of different ions in the simulational cell depend on the cell size, salt concentration, and helix length. The two helices are placed at the center of the cell, and the helices are kept fixed and the ions are allowed to move.

The electrostatic potential energy for a given ion distribution of the system is computed as the sum of the Coulombic interactions (83,108),

$$E_p = \sum_i \sum_{j=i+1} \frac{z_i z_j q^2}{\epsilon r_{ij}} + \sum_i \sum_l \frac{z_i z_l q^2}{\epsilon r_{il}},$$

where i denotes ions in the cell, $j(\neq i)$ denotes ions in the cell and in the image cells, l denotes the phosphate groups, and z_iq, z_jq, and z_lq are the charges of the respective ions and the phosphate groups. The first double summation accounts for the interactions between ions in the cell and all other ions (in the cell and the adjacent image cells). The second double summation accounts for the interactions between ions in the cell and the phosphate charges on the nucleic acid backbones. Following the simulation algorithm in Tan and Chen (83) and Olmsted et al. (108), we consider only the nearest adjacent image cells.

For each Monte Carlo move of the ions, we compute the energy change $\Delta E(= \Delta E_p + \Delta E_k)$ of the system, and the acceptable probability $\exp(-\Delta E/k_BT)$ for the particular move. Here, E_k is the kinetic energy in which the velocity components are drawn from a Gaussian distribution (for details, see (122)). The ions are simulated to move with the acceptable probabilities. Such a stochastic move process continues until the system reaches thermal equilibrium, from which the equilibrium properties of the system can be calculated.

We are grateful to Dr. Donald C. Rau for valuable discussions on DNA-DNA interactions.

This research was supported by National Institutes of Health through grant No. GM063732 (to S.-J.C.).

REFERENCES

1. Bloomfield, V. A., D. M. Crothers, and I. Tinoco, Jr. 2000. Nucleic Acids: Structure, Properties and Functions. University Science Books, Sausalito, CA.
2. Tinoco, I., and C. Bustamante. 1999. How RNA folds. *J. Mol. Biol.* 293:271–281.
3. Anderson, C. F., and M. T. Record, Jr. 1995. Salt-nucleic acid interactions. *Annu. Rev. Phys. Chem.* 46:657–700.
4. Sosnick, T. R., and T. Pan. 2003. RNA folding: models and perspectives. *Curr. Opin. Struct. Biol.* 13:309–316.
5. Woodson, S. A. 2005. Metal ions and RNA folding: a highly charged topic with a dynamic future. *Curr. Opin. Chem. Biol.* 9:104–109.
6. Draper, D. E., D. Grilley, and A. M. Soto. 2005. Ions and RNA folding. *Annu. Rev. Biophys. Biomol. Struct.* 34:221–243.

7. Cate, J. H., A. R. Gooding, E. Podell, K. Zhou, B. L. Golden, C. E. Kundrot, T. R. Cech, and J. A. Doudna. 1996. Crystal structure of a group I ribozyme domain: principles of RNA packing. *Science*. 273: 1678–1685.
8. Thirumalai, D., and C. Hyeon. 2005. RNA and protein folding: common themes and variations. *Biochemistry*. 44:4957–4970.
9. Rook, M. S., D. K. Treiber, and J. R. Williamson. 1999. An optimal Mg^{2+} concentration for kinetic folding of the *Tetrahymena* ribozyme. *Proc. Natl. Acad. Sci. USA*. 96:12471–12476.
10. Misra, V. K., and D. E. Draper. 2001. A thermodynamic framework for Mg^{2+} binding to RNA. *Proc. Natl. Acad. Sci. USA*. 98:12456–12461.
11. Freier, S. M., R. Kierzek, J. A. Jaeger, N. Sugimoto, M. H. Caruthers, T. Neilson, and D. H. Turner. 1986. Improved free-energy parameters for predictions of RNA duplex stability. *Proc. Natl. Acad. Sci. USA*. 83:9373–9377.
12. Breslauer, K. J., R. Frank, H. Blocker, and L. A. Marky. 1986. Predicting DNA duplex stability from the base sequence. *Proc. Natl. Acad. Sci. USA*. 83:3746–3750.
13. SantaLucia, J., Jr., and D. Hicks. 2004. The thermodynamics of DNA structural motifs. *Annu. Rev. Biophys. Biomol. Struct.* 33:415–440.
14. Sugimoto, N., S. I. Nakano, M. Yoneyama, and K. T. Honda. 1996. Improved thermodynamic parameters and helix initiation factor to predict stability of DNA duplexes. *Nucleic Acids Res*. 24:4501–4505.
15. Owczarzy, R., P. M. Callone, F. J. Gallo, T. M. Paner, M. J. Lane, and A. S. Benight. 1997. Predicting sequence-dependent melting stability of short duplex DNA oligomers. *Biopolymers*. 44:217–239.
16. Mathews, D. H., J. Sabina, M. Zuker, and D. H. Turner. 1999. Expanded sequence dependence of thermodynamic parameters improves prediction of RNA secondary structure. *J. Mol. Biol.* 288:911–940.
17. Yildirim, I., and D. H. Turner. 2005. RNA challenges for computational chemists. *Biochemistry*. 44:13225–13234.
18. Chen, S. J., and K. A. Dill. 2000. RNA folding energy landscapes. *Proc. Natl. Acad. Sci. USA*. 97:646–651.
19. Zhang, W. B., and S. J. Chen. 2002. RNA hairpin-folding kinetics. *Proc. Natl. Acad. Sci. USA*. 99:1931–1936.
20. Heilman-Miller, S. L., D. Thirumalai, and S. A. Woodson. 2001. Role of counterion condensation in folding of the *Tetrahymena* ribozyme. I. Equilibrium stabilization by cations. *J. Mol. Biol.* 306:1157–1166.
21. Heilman-Miller, S. L., J. Pan, D. Thirumalai, and S. A. Woodson. 2001. Role of counterion condensation in folding of the *Tetrahymena* ribozyme. II. Counterion-dependence of folding kinetics. *J. Mol. Biol.* 309:57–68.
22. Koculi, E., N.-K. Lee, D. Thirumalai, and S. A. Woodson. 2004. Folding of the *Tetrahymena* ribozyme by polyamines: importance of counterion valence and size. *J. Mol. Biol.* 341:27–36.
23. Takamoto, K., Q. He, S. Morris, M. R. Chance, and M. Brenowitz. 2002. Monovalent cations mediate formation of native tertiary structure of the *Tetrahymena thermophila* ribozyme. *Nat. Struct. Biol*. 9: 928–933.
24. Fang, X., T. Pan, and T. R. Sosnick. 1999. A thermodynamic framework and cooperativity in the tertiary folding of a Mg^{2+}-dependent ribozyme. *Biochemistry*. 38:16840–16846.
25. Buchmueller, K. L., A. E. Webb, D. A. Richardson, and K. M. Weeks. 2000. A collapsed non-native RNA folding state. *Nat. Struct. Biol.* 7:362–366.
26. Russell, R., I. S. Millett, S. Doniach, and D. Herschlag. 2002. Small angle x-ray scattering reveals a compact intermediate in RNA folding. *Nat. Struct. Biol.* 7:367–370.
27. Russell, R., I. S. Millett, M. W. Tate, L. W. Kwok, B. Nakatani, S. M. Gruner, S. G. J. Mochrie, V. Pande, S. Doniach, D. Herschlag, and L. Pollack. 2002. Rapid compaction during RNA folding. *Proc. Natl. Acad. Sci. USA*. 99:4266–4271.
28. Das, R., L. W. Kwok, I. S. Millett, Y. Bai, T. T. Mills, J. Jacob, G. S. Maskel, S. Seifert, S. G. J. Mochrie, P. Thiyagarajan, S. Doniach, L. Pollack, and D. Herschlag. 2003. The fastest global events in RNA folding: electrostatic relaxation and tertiary collapse of the *Tetrahymena* ribozyme. *J. Mol. Biol.* 332:311–319.
29. Bai, Y., R. Das, I. S. Millett, D. Herschlag, and S. Doniach. 2005. Probing counterion modulated repulsion and attraction between nucleic acid duplexes in solution. *Proc. Natl. Acad. Sci. USA*. 102:1035–1040.
30. Bloomfield, V. A. 1997. DNA condensation by multivalent cations. *Biopolymers*. 44:269–282.
31. Wilson, R. W., and V. A. Bloomfield. 1979. Counterion-induced condensation of deoxyribonucleic acid. a light-scattering study. *Biochemistry*. 18:2192–2196.
32. Widom, J., and R. L. Baldwin. 1980. Cation-induced toroidal condensation of DNA studies with $Co^{3+}(NH_3)_6$. *J. Mol. Biol.* 144:431–453.
33. Schellman, J. A., and N. Parthasarathy. 1984. X-ray diffraction studies on cation-collapsed DNA. *J. Mol. Biol.* 175:313–329.
34. Ma, C., and V. A. Bloomfield. 1994. Condensation of supercoiled DNA induced by $MnCl_2$. *Biophys. J.* 67:1678–1681.
35. Arscott, P. G., C. Ma, J. R. Wenner, and V. A. Bloomfield. 1995. DNA condensation by cobalt hexamine (III) in alcohol-water mixtures: dielectric constant and other solvent effects. *Biopolymers*. 36: 345–364.
36. Pelta, J., F. Livolant, and J. L. Sikorav. 1996. DNA aggregation induced by polyamines and cobalt hexamine. *J. Biol. Chem.* 271: 5656–5662.
37. Raspaud, E., M. O. de la Cruz, J. L. Sikorav, and F. Livolant. 1998. Precipitation of DNA by polyamines: a polyelectrolyte behavior. *Biophys. J.* 74:381–393.
38. Koltover, I., K. Wagner, and C. R. Safinya. 2000. DNA condensation in two dimensions. *Proc. Natl. Acad. Sci. USA*. 97:14046–14051.
39. Vijayanathan, V., T. Thomas, A. Shirahata, and T. J. Thomas. 2001. DNA condensation by polyamines: a laser light scattering study of structural effects. *Biochemistry*. 40:13644–13651.
40. Conwell, C. C., ID Vilfan, and N. V. Hud. 2003. Controlling the size of nanoscale toroidal DNA condensates with static curvature and ionic strength. *Proc. Natl. Acad. Sci. USA*. 100:9296–9301.
41. Tang, J. X., and P. A. Janmey. 1996. The polyelectrolyte nature of F-actin and the mechanism of actin bundle formation. *J. Biol. Chem.* 271:8556–8563.
42. Tang, J. X., S. Wong, P. T. Tran, and P. A. Janmey. 1996. Counterion-induced bundle formation of rodlike polyelectrolyte. *Ber. Bunsenges. Phys. Chem.* 100:796–806.
43. de Frutos, M., E. Raspaud, A. Leforestier, and F. Livolant. 2001. Aggregation of nucleosomes by divalent cations. *Biophys. J.* 81:1127–1132.
44. Tang, J. X., P. A. Janmey, A. Lyubartsev, and L. Nordenskiold. 2002. Metal ion-induced lateral aggregation of filamentous viruses fd and M13. *Biophys. J.* 83:566–581.
45. Butler, J. C., T. Angelini, J. X. Tang, and G. C. Wong. 2003. Ion multivalence and like-charge polyelectrolyte attraction. *Phys. Rev. Lett*. 91:028301.
46. Angelini, T. E., H. Liang, W. Wriggers, and G. C. Wong. 2003. Like-charge attraction between polyelectrolytes induced by counterion charge density waves. *Proc. Natl. Acad. Sci. USA*. 100:8634–8637.
47. Wen, Q., and J. X. Tang. 2004. Absence of charge inversion on rodlike polyelectrolytes with excess divalent counterions. *J. Chem. Phys.* 121:12666–12670.
48. Gilson, M. K., K. A. Sharp, and B. Honig. 1987. Calculating the electrostatic potential of molecules in solution: method and error assessment. *J. Comput. Chem*. 9:327–335.
49. Sharp, K. A., and B. Honig. 1990. Calculating total electrostatic energies with the nonlinear Poisson-Boltzmann equation. *J. Phys. Chem*. 94:7684–7692.
50. Nicholls, A., and B. Honig. 1991. A rapid finite-difference algorithm, utilizing successive over-relaxation to solve the Poisson-Boltzmann equation. *J. Comput. Chem*. 12:435–445.

51. You, T. J., and S. C. Harvey. 1993. Finite element approach to the electrostatics of macromolecules with arbitrary geometries. *J. Comput. Chem.* 14:484–501.
52. Baker, N. A., D. Sept, S. Joseph, M. J. Holst, and J. A. McCammon. 2000. Electrostatics of nanosystems: application to microtubules and the ribosome. *Proc. Natl. Acad. Sci. USA.* 98:10037–10041.
53. Grant, J. A., B. T. Pickup, and A. Nicholls. 2001. A smooth permittivity function for Poisson-Boltzmann solvation methods. *J. Comput. Chem.* 22:608–640.
54. Sept, D., N. A. Baker, and J. A. McCammon. 2003. The physical basis of microtubule structure and stability. *Protein Sci.* 12:2257–2261.
55. Baker, N. A. 2005. Improving implicit solvent simulations: a Poisson-centric view. *Curr. Opin. Struct. Biol.* 15:137–143.
56. Manning, G. S. 1978. The molecular theory of polyelectrolyte solutions with applications to the electrostatic properties of polynucleotides. *Q. Rev. Biophys.* 2:179–246.
57. Oosawa, F. 1971. Polyelectrolytes. Marcel Dekker, New York.
58. Ray, J., and G. S. Manning. 1994. An attractive force between two rodlike polyions mediated by the sharing of condensed counterions. *Langmuir.* 10:2450–2461.
59. Ray, J., and G. S. Manning. 2000. Formation of loose clusters in polyelectrolyte solutions. *Macromolecules.* 33:2901–2908.
60. Manning, G. S. 2003. Comments on selected aspects of nucleic acid electrostatics. *Biopolymers.* 69:137–143.
61. Murthy, V. L., and G. D. Rose. 2000. Is counterion delocalization responsible for collapse in RNA folding? *Biochemistry.* 39:14365–14370.
62. Lyubartsev, A. P., and L. Nordenskiold. 1995. Monte Carlo simulation study of ion distribution and osmotic pressure in hexagonally oriented DNA. *J. Phys. Chem.* 99:10373–10382.
63. Gronbech-Jensen, N., R. J. Mashl, R. F. Bruinsma, and W. M. Gelbart. 1997. Counterion-induced attraction between rigid polyelectrolytes. *Phys. Rev. Lett.* 78:2477–2480.
64. Wu, J. Z., D. Bratko, H. W. Blanch, and J. M. Prausnitz. 1999. Monte Carlo simulation for the potential of mean force between ionic colloids in solutions of asymmetric salts. *J. Chem. Phys.* 111:7084–7094.
65. Wu, J. Z., D. Bratko, and J. M. Prausnitz. 1998. Interaction between like-charged colloidal spheres in electrolyte solutions. *Proc. Natl. Acad. Sci. USA.* 95:15169–15172.
66. Messina, R., C. Holm, and K. Kremer. 2000. Strong attraction between charged spheres due to metastable ionized states. *Phys. Rev. Lett.* 85:872–875.
67. Stevens, M. J. 2001. Simple simulations of DNA condensation. *Biophys. J.* 80:130–139.
68. Lee, N., and D. Thirumalai. 2001. Dynamics of collapse of flexible polyelectrolytes in poor solvents. *Macromolecules.* 34:3446–3457.
69. Deserno, M., A. Arnold, and C. Holm. 2003. Attraction and ionic correlations between charged stiff polyelectrolytes. *Macromolecules.* 36:249–259.
70. Allahyarov, E., G. Gompper, and H. Lowen. 2004. Attraction between DNA molecules mediated by multivalent ions. *Phys. Rev. E.* 69:041904.
71. Lee, K. C., I. Borukhov, W. M. Gelbart, A. J. Liu, and M. J. Stevens. 2004. Effect of mono- and multivalent salts on angle-dependent attractions between charged rods. *Phys. Rev. Lett.* 93:128101.
72. Ou, Z., and M. Muthukumar. 2005. Langevin dynamics of semiflexible polyelectrolytes: rod-toroid-globule-coil structures and counterion distribution. *J. Chem. Phys.* 123:074905.
73. Rouzina, I., and V. A. Bloomfield. 1996. Macroion attraction due to electrostatic correlation between screening counterions. 1. Mobile surface-adsorbed ions and diffuse ion cloud. *J. Phys. Chem.* 100: 9977–9989.
74. Ha, B. Y., and A. J. Liu. 1997. Counterion-mediated attraction between two like-charged rods. *Phys. Rev. Lett.* 79:1289–1292.
75. Podgornik, R., and V. A. Parsegian. 1998. Charge-fluctuation forces between rodlike polyelectrolytes: pairwise summability reexamined. *Phys. Rev. Lett.* 80:1560–1563.
76. Solis, F. J., and M. O. de la Cruz. 1999. Attractive interactions between rodlike polyelectrolytes: polarization, crystallization, and packing. *Phys. Rev. E.* 60:4496–4499.
77. Kornyshev, A. A., and S. Leikin. 1999. Electrostatic zipper motif for DNA aggregation. *Phys. Rev. Lett.* 82:4138–4141.
78. Shklovskii, B. I. 1999. Wigner crystal model of counterion induced bundle formation of rodlike polyelectrolytes. *Phys. Rev. Lett.* 82:3268–3271.
79. Arenzon, J. J., J. F. Stilck, and Y. Levin. 1999. Simple model for attraction between like-charged polyions. *Eur. Phys. J. B.* 12:79–82.
80. Lau, A. W. C., D. Levine, and P. Pincus. 2000. Novel electrostatic attraction from plasmon fluctuations. *Phys. Rev. Lett.* 84:4116–4119.
81. Yu, X., and A. E. Carlsson. 2003. Multiscale study of counterion-induced attraction and bundle formation of F-actin using an Ising-like mean-field model. *Biophys. J.* 85:3532–3543.
82. Naji, A., and R. R. Netz. 2004. Attraction of like-charged macroions in the strong-coupling limit. *Eur. Phys. J. E.* 13:43–59.
83. Tan, Z. J., and S. J. Chen. 2005. Electrostatic correlations and fluctuations for ion binding to a finite length polyelectrolyte. *J. Chem. Phys.* 122:044903.
84. Tan, Z. J., and S. J. Chen. 2006. Nucleic acid helix stability: effects of salt concentration, cation valency and size, and chain length. *Biophys. J.* 90:1175–1190.
85. Pollock, E., and J. Hansen. 1973. Statistical mechanics of dense ionized matter. II. Equilibrium properties and melting transition of the crystallized one-component plasma. *Phys. Rev. A.* 8:3110–3122.
86. Slattery, W., G. Doolen, and H. Dewitt. 1980. Improved equation of state for the classical one-component plasma. *Phys. Rev. A.* 21:2087–2095.
87. Ichimaru, S., H. Iyetomi, and S. Tanaka. 1987. Statistical physics of dense plasmas: thermodynamics, transport coefficients and dynamic correlations. *Phys. Rep.* 149:91–205.
88. Lindemann, F. A. 1910. The calculation of molecular vibration frequencies. *Z. Phys.* 11:609–612.
89. Zhou, Y., M. Karplus, K. D. Ball, and R. S. Berry. 2002. The distance fluctuation criterion for melting: comparison of square-well and Morse potential models for clusters and homopolymers. *J. Chem. Phys.* 116: 2323–2329.
90. Truskett, T. M., S. Torquato, S. Sastry, P. G. Debenedetti, and F. H. Stillinger. 1998. Structural precursor to freezing in the hard-disk and hard sphere systems. *Phys. Rev. E.* 58:3083–3088.
91. Overbeek, J. T. G. 1990. The role of energy and entropy in the electrical double layer. *Coll. Surf.* 51:61–75.
92. Stigter, D. 1995. Evaluation of the counterion condensation theory of polyelectrolytes. *Biophys. J.* 69:380–388.
93. Raspaud, E., D. Durand, and F. Livolant. 2005. Interhelical spacing in liquid crystalline spermine and spermidine-DNA precipitates. *Biophys. J.* 88:392–403.
94. Nguyen, T. T., I. Rouzina, and B. I. Shklovskii. 2000. Reentrant condensation of DNA induced by multivalent counterions. *J. Chem. Phys.* 112:2562–2568.
95. Yang, J., and D. C. Rau. 2005. Incomplete ion dissociation underlies the weakened attraction between DNA helices at high spermidine concentrations. *Biophys. J.* 89:1932–1940.
96. Rau, D. C., and V. A. Parsegian. 1992. Direct measurement of the intermolecular forces between counterion-condensed DNA double helices. Evidence for long range attractive hydration forces. *Biophys. J.* 61:246–259.
97. Rau, D. C., and V. A. Parsegian. 1992. Direct measurement of temperature-dependent solvation forces between DNA double helices. *Biophys. J.* 61:260–271.
98. Hackl, E. V., S. V. Kornilova, and Y. P. Blagoi. 2005. DNA structural transitions induced by divalent metal ions in aqueous solutions. *Int. J. Biol. Macromol.* 35:175–191.
99. Hackl, E. V., and Y. P. Blagoi. 2005. The effect of temperature on DNA structural transitions under the action of Cu^{2+} and Ca^{2+} ions in aqueous solutions. *Biopolymers.* 77:315–324.

100. Marcus, Y. 1985. Ion Solvation. John Wiley & Sons Ltd., Great Britain.

101. Cherstvy, A. G., A. A. Kornyshev, and S. Leikin. 2002. Temperature-dependent DNA condensation triggered by rearrangement of adsorbed cations. *J. Phys. Chem. B.* 106:13362–13369.

102. Stigter, D. 1998. An electrostatic model for the dielectric effects, the adsorption of multivalent ions, and the bending of B-DNA. *Biopolymers.* 46:503–516.

103. Rouzina, I., and V. A. Bloomfield. 1998. DNA bending by small, mobile multivalent cations. *Biophys. J.* 74:3152–3164.

104. Young, M. A., B. Jayaram, and D. L. Beveridge. 1998. Local dielectric environment of B-DNA in solution: results from a 14 ns molecular dynamic trajectory. *J. Phys. Chem. B.* 102:7666–7669.

105. Ramstein, J., and R. Lavery. 1988. Energetic coupling between DNA bending and base pair opening. *Proc. Natl. Acad. Sci. USA.* 85:7231–7235.

106. Flock, S., R. Labarbe, and C. Houssier. 1996. Dielectric constant and ionic strength effects on DNA precipitation. *Biophys. J.* 70:1456–1465.

107. Flock, S., R. Labarbe, and C. Houssier. 1995. Osmotic effectors and DNA structure: effect of glycine on precipitation of DNA by multivalent cations. *J. Biomol. Struct. Dyn.* 13:87–102.

108. Olmsted, M. C., C. F. Anderson, and M. T. Record, Jr. 1989. Monte Carlo description of oligoelectrolyte properties of DNA oligomers: range of the end effect and the approach of molecular and thermodynamic properties to the polyelectrolyte limits. *Proc. Natl. Acad. Sci. USA.* 86:7766–7770.

109. Ballin, J. D., I. A. Shkel, and M. T. Record, Jr. 2004. Interactions of the KWK6 cationic peptide with short nucleic acid oligomers: demonstration of large Coulombic end effects on binding at 0.1–0.2 M salt. *Nucleic Acids Res.* 32:3271–3281.

110. Zhang, W., H. Ni, M. W. Capp, C. F. Anderson, T. M. Lohman, and M. T. Record, Jr. 1999. The importance of Coulombic end effects: experimental characterization of the effects of oligonucleotide flanking charges on the strength and salt dependence of oligocation ($L8^+$) binding to single-stranded DNA oligomers. *Biophys. J.* 76: 1008–1017.

111. Rau, D. C., B. Lee, and V. A. Parsegian. 1984. Measurement of the repulsive force between polyelectrolyte molecules in ionic solution: hydration forces between parallel DNA double helices. *Proc. Natl. Acad. Sci. USA.* 81:2621–2625.

112. Podgornik, R., D. C. Rau, and V. A. Parsegian. 1994. Parameterization of direct and soft steric-undulatory forces between DNA double helical polyelectrolytes in solutions of several different anions and cations. *Biophys. J.* 66:962–971.

113. Henle, M. L., and P. A. Pincus. 2005. Equilibrium bundle size of rodlike polyelectrolytes with counterion-induced attractive interactions. *Phys. Rev. E.* 71:060801.

114. Duguid, J., V. A. Bloomfield, J. Benevides, and G. J. Thomas. 1993. Raman spectroscopy of DNA-metal complexes. I. Interactions and conformational effects of the divalent cations: Mg, Ca, Sr, Ba, Mn, Co, Ni, Cu, Pd, and Cd. *Biophys. J.* 65:1916–1928.

115. Andrushchenko, V., H. van de Sande, and H. Wieser. 2003. DNA interaction with Mn^{2+} ions at elevated temperatures: VCD evidence of DNA aggregation. *Biopolymers.* 69:529–545.

116. Devarajan, S., N. Pattabiraman, and R. H. Shafer. 1988. Effect of discrete distribution of ions on B- and Z-DNA: a theoretical investigation. *Biopolymers.* 27:187–200.

117. Saenger, W. 1984. Principles of Nucleic Acid Structure. Springer-Verlag, New York. 298–320.

118. Montoro, J. C. G., and J. L. F. Abascal. 1995. Ionic distribution around simple DNA models. I. Cylindrically averaged properties. *J. Chem. Phys.* 103:8273–8284.

119. Arnott, S., and D. W. L. Hukins. 1972. Optimised parameters for A-DNA and B-DNA double-helices. *Biochem. Biophys. Res. Commun.* 47:1504–1509.

120. Dwyer, J. J., A. G. Gittis, D. A. Karp, E. E. Lattman, D. S. Spencer, W. E. Stites, and B. E. Garcia-Moreno. 2000. High apparent dielectric constants in the interior of a protein reflect water penetration. *Biophys. J.* 79:1610–1620.

121. Eisenberg, D., and W. Kauzmann. 1969. The Structure and Properties of Water. Oxford University Press, Oxford.

122. Schlick, T. 2002. Molecular Modeling and Simulation. Springer-Verlag, New York.

123. Duane, S., A. D. Kennedy, B. J. Pendleton, and D. Roweth. 1987. Hybrid Monte Carlo. *Phys. Lett. B.* 195:216–222.

124. Berne, B. J., and J. E. Straub. 1997. Novel methods of sampling phase space in the simulation of biological systems. *Curr. Opin. Struct. Biol.* 7:181–189.

125. Kwok, L. W., I. Shcherbakova, J. S. Lamb, H. Y. Park, K. Andresen, H. Smith, M. Brenowitz, and L. Pollack. 2006. Concordant exploration of the kinetics of RNA folding from global and local perspectives. *J. Mol. Biol.* 355:282–293.